UNIVERSITY OF CALIFORNIA SAN DIEGO

Planar Biaxial Mechanical Testing of Rat Right Ventricular Myocardium for Characterization of Sex Differences in PAH

A thesis submitted in partial satisfaction of the
requirements for the degree Master of Science

in

Bioengineering

by

Jessica Huberts

Committee in charge:

Professor Daniela Valdez-Jasso, Chair
Professor Andrew Douglas McCulloch
Professor Jeffrey Howard Omens

2023

The Thesis of Jessica Huberts is approved, and it is acceptable in quality and form for publication on microfilm and electronically.

University of California San Diego

2023

TABLE OF CONTENTS

LIST OF FIGURES

LIST OF TABLES

ACKNOWLEDGEMENTS

I would first like to acknowledge Dr. Daniela Valdez-Jasso for her unending mentorship and support throughout my graduate studies, as well as for welcoming me warmly into her lab and giving me the opportunity to grow as a student, researcher, and person.

A second thanks goes to Becky Hardie, who's mentorship and friendship made this work fun, and so much easier than if I'd had to figure it out on my own. Another special thanks to Parisa Shahabi for invaluable help collecting and analyzing data. Thank you to the rest of the DVJ Lab for providing me a fun and supportive working and learning environment. Kristen Garcia, Hao Mu, Ethan Kwan, Vaishali Harimani, Yufan Lin, and Sarita Giri kept long days interesting, and were always willing and eager to help.

I would also like to thank Dr. Andrew McCulloch and Dr. Jeff Omens for their advice and support in finishing and defending my thesis.

Profound thanks to my family for their unwavering confidence in me, and for the years of teaching and nurturing that led up to this; they encouraged me to aim high and keep going higher. Thank you to my close and significant friends for making me laugh every day, no matter how arduous the circumstance.

Finally, I would like to thank the many rats that made this research possible.

ABSTRACT OF THE THESIS

Planar Biaxial Mechanical Testing of Rat Right Ventricular Myocardium for Characterization of Sex Differences in PAH

by

Jessica Huberts

Master of Science in Bioengineering

University of California San Diego, 2023

Professor Daniela Valdez-Jasso, Chair

Pulmonary arterial hypertension (PAH) is a progressive vasculopathy characterized by elevated pressures and remodeling in the pulmonary arteries, leading to an overloaded right ventricle (RV) and eventual right heart failure, making RV function a key indicator of the disease. PAH exhibits a strong sexual dimorphism, where females are more frequently afflicted with the disease, but pre-menopausal women tend to have better survival outcomes. Many studies have investigated how the RV adapts in PAH, and others have looked for mechanisms behind the so-called sex-paradox, but the reason females have a survival advantage is unclear. In this thesis, the remodeling process of the RV was quantified along the time-progression of PAH

in male, intact female, and ovariectomized (OVX) female rats treated with Sugen-Hypoxia (SuHx). Planar biaxial mechanical testing of the RV myocardium was performed to generate stress-strain relationships, which were then fit to a Fung-type exponential strain energy model to generate surfaces for group averaging and comparison. RV samples were decellularized and retested to characterize the mechanical behavior of the collagen extracellular matrix (ECM), and collagen content was quantified in distinct regions of the RV myocardium. It was shown that, in normotension, the RV behaves preferentially in the apex-outflow direction in control males, but isotropically in female rats. In SuHx-PAH, the RV shows enlarged thickness and mass, and increased stiffness compared to controls; however, this remodeling is sex-specific, with RV myocardium and collagen ECM from intact females stiffening the least. As the disease progresses, we see male and intact female RVs reach peak stiffness at 8 weeks of PAH, while OVX female RVs stiffen more in early weeks of the disease and maintain that stiffening through the late stage. Collagen content increases in PAH, with regional variation. This study can be used as a quantitative reference for RV passive stiffening in the SuHx rat model of PAH, and findings of differences in the collagen ECM may help future studies identify underlying mechanisms of differential RV stiffening between sexes.

Chapter 1

Background and Significance

1.1 Pulmonary Arterial Hypertension (PAH)

1.1.1 Disease Definition, Classifications, and Epidemiology

Pulmonary arterial hypertension (PAH) is a rare progressive vasculopathy characterized by sustained elevated pressures and structural remodeling in the pulmonary arteries. It is clinically diagnosed by a resting mean pulmonary arterial pressure (mPAP) of ≥ 20 mmHg and in late-stage disease progression, has characteristic vascular changes such as the formation of plexiform lesions and in situ thromboembolism [1] [2]. These changes lead to an increased pulmonary vascular resistance (PVR) which results in an increased load on the right ventricle (RV), making RV function a key indicator of the disease.

PAH is a sub-classification of the broader group of disorders known as pulmonary hypertension (PH), which also includes PH due to left heart disease, PH due to lung diseases and/or hypoxia, PH due to pulmonary artery obstructions, and PH with unclear and/or multifactorial mechanisms [3]. Within the PAH group, there are further subgroups: idiopathic PAH, heritable PAH, drug/toxin-induced PAH, and PAH associated with other medical conditions [3]. Diagnosis of PAH must be confirmed via right heart catheterization, but typically includes a combination of tests not limited to history, physical exam, and laboratory screening [2]. Symptoms of PAH can be vague and are often misdiagnosed, but commonly include dyspnea (or shortness of breath), fatigue, and weakness [3].

Available data on PAH prevalence in adults gives an estimated range of 47.6–54.7 per million, though there is wide variation in published estimates which could indicate geographic differences, possibly due to racial and ethnic differences or differences in routine clinical practices [4]. While some more recent reports from clinical trials suggest improvement in survival with modern treatments, the mortality rate at 3 years for patients with PAH is historically approximated at 50% [2].

PAH currently remains an incurable disorder, with severe cases sometimes requiring heart-lung transplant as an extreme treatment option. There are, however, several pharmacotherapies available that aim to manage symptoms and improve survival for patients with less-severe cases. These include prostacyclin pathway inhibitors such as epoprostenol, which cause vasodilation of the pulmonary vessels; endothelin receptor inhibitors such as bosentan, which block constriction of the vessels; nitric oxide-cyclic guanosine monophosphate (NO-cGMP) enhancers, which again promote vasodilation; and, rarely, calcium channel blockers [3]. Several animal studies have suggested that the use of estrogenic hormones in treatment of PAH can have both protective and rescuing affects on lung and RV outcomes, but the role of estrogen in human PAH is unclear and remains an active area of research [5] [6] [7] [8].

1.1.2 RV Prognosis

The RV functions to maintain cardiac output (CO) through the lungs, a vascular system that in healthy individuals has low pressure and high flow. The elevated pressures and structural remodeling in the pulmonary arteries seen in PAH cause a progressive increase in PVR, which in turn leads to RV remodeling and eventual right heart failure. This remodeling is at first adaptive and acts to maintain cardiac demands. Adaptive RV remodeling includes structural changes, neurohormonal activation, and increased contractility, which arise from a series of cellular-level changes [9]. Over time, further changes in the RV lead to reduced contractile function, decreased CO, and decreased oxygen delivery, and these changes represent a transition to maladaptive remodeling [9] [10]. This transition from adaptive to maladaptive remodeling is

an incompletely-understood pathobiological occurrence that requires further biomechanical and biochemical research and analysis to properly characterize.

Despite these gaps in the current knowledge, RV function remains an important clinical tool for evaluating PAH severity and has several well-characterized changes in the disease state. RV systolic adaptation includes an increase in systolic elastance explained by increased muscle mass and enhanced myocyte contractility [11]; but, these changes can have diastolic consequences: increased stiffness and impaired relaxation due to cardiomyocyte hypertrophy and fibrosis [12]. These changes have been observed in both human and animal studies of PAH, and represent an active area of research [12] [11] [13].

Recent attempts to differentiate the contributions of geometric remodeling versus alterations to material properties on changes in RV chamber function found the latter to be responsible for increased RV end-diastolic pressures in male rats – specifically an increase in passive myocardial stiffness [14]. This increase in stiffness was not linked to significant changes in fibrosis or collagen content [14]. Previously, the increase in male RV stiffness in PAH was explained by an increase in stiffness of the extracellular matrix (ECM) [15].

1.1.3 Sex Differences in PAH

PAH exhibits a strong and perplexing sexual dimorphism in its penetrance, presentation, and progression: the disease occurs more frequently in women, however, women tend to have better survival outcomes. Earliest registry data demonstrated a female:male ratio of 1.7:1 [16], with modern registry ratios varying widely between demographics and over time, ranging as high as 5.4:1 in African Americans in the 2010 REVEAL registry [17]. This difference in prevalence appears to diminish with age, with studies reporting a reduction in female/male differences occurring between the ages of 45 and 65, suggesting a complex interaction between sex, age, and hormones [18] [19]. Pre-menopausal women exhibit better RV function, hemodynamic profile, and treatment response compared to men, but the reason females have a survival advantage is unclear; thus exists what is referred to as the sex- or estrogen-paradox in PAH [20].

In the RV, female sex is associated with better systolic function both in health and in PAH [19]. Healthy (free of cardiovascular disease) women who use hormone therapy were found to have preferable RV systolic function, which was associated with higher levels of estradiol [21]. Similar sex differences have been observed in patients with PAH, where female sex has been associated with higher right-ventricular ejection fraction (RVEF) compared to males, despite similar increases in PVR [19]. Studies in rats have sought to identify a more specific mechanism driving these differences, and have looked to the effects of 17β-Estradiol (E2) on RV chamber function. Frump *et al.* demonstrated that sex differences do exist in RV function for a preclinical rat model, where females performed better than males, and that ovariectomy worsens disease progression in the RV, but its effects can be improved with E2 repletion, which was further linked to attenuation of maladaptive processes [7]. Similarly, Lahm *et al.* studied the effects of exercise on RV function in male, intact female, and ovariectomized (OVX) female PAH rats, where the OVX group was additionally treated with or without E2 repletion, and found that both endogenous and exogenous E2 has protective effects on RV function [22]. These works indicate that sex and estrogen are important factors in the progression of RV adaptation in PAH, but further investigation is needed to fully elucidate the nature of mechanical changes that occur in the disease.

1.1.4 Animal Models of PAH

Various animal models have been used in the study of PAH, but due to its complex and multifactorial nature, no single one fully reproduces all characteristics of the disease. This section will briefly cover some of the more popular animal models for PAH, with special attention paid to the Sugen-Hypoxia (SuHx) rat model – the model of choice in the following project. While some PAH research has been done using larger mammals such as chicken, sheep, and pigs, rodent models are far more popular due to their feasibility, well-documented genetics, and ability to closely imitate human diseases [20]. Mouse models present many options for the study of genes and gene expression in PAH, specifically the hereditary sub-type, but these models typically

have variable penetrance and require additional stressors such as exposure to hypoxia in order to reproduce the disease [23]. Newer technology has allowed for the recent development of a mutant rat model for PAH, but similar issues occurred, making it sub-optimal [24].

Rats are favored over mice in much of PAH research, in part due to the technical challenges involved with studying the pulmonary vasculature and RV functions in mice, but also due to their ability to successfully mimic many aspects of the human disease. Injection of monocrotaline (MCT) is one of the most popular methods of PAH induction in rats. This model is well-established as a means to produce pulmonary vascular remodeling, and in turn, elevated pulmonary artery (PA) pressure and RV dysfunction in rats; a single subcutaneous injection results in acute PA injury, followed by an inflammatory response in the lungs and progressive vasculopathy, and finally ending in death within weeks [25]. However, MCT rats do not display plexiform lesions, an important characteristic of human PAH, unless the model is combined with exposure to chronic hypoxia or pneumonectomy [25], and then there is still the issue of prompt death, which makes longitudinal studies challenging in this model.

Prior to MCT, chronic hypoxia was a commonly used model for PAH, however, this model did not produce PAH to a comparable severity as is seen in humans and is reversible upon return to normoxia [25]. The SuHx model was thus developed following findings that the vascular endothelial growth factor (VEGF) receptor inhibitor sugen 5416 causes pulmonary endothelial cell apoptosis and PA pruning, and later, that combination with chronic hypoxia causes severe, irreversible pulmonary hypertension that continues to worsen after removal from hypoxia and includes plexiform-like lesions that closely resemble those found in humans [26] [27] [28]. Toba *et al.* studied the temporal progression of PAH in adult male Sprague-Dawley rats and found that, following a single sugen injection plus three weeks in hypoxic conditions, occlusion of small PAs and increase of RV systolic pressure occurred in a manner similar to human PAH patients [29]. These features make the SuHx rat model a popular option in PAH research, and the model of choice for our experiments.

1.2 Engineering Background

1.2.1 Planar Biaxial Mechanical Testing

The primary physiological and engineering focus of this project is to characterize the tissue-level mechanical properties of the right ventricle. Given the thin ventricle, planar biaxial mechanical testing is considered a good approach. Prior to the development of systems for planar biaxial testing, uniaxial testing was commonly used for the study of mechanical tissue properties; however, these tests fall short in their capacity to capture and characterize anisotropy and complex multi-dimensional behaviors that are more relevant to the way tissues like the myocardium behave in the body. Biaxial testing has origins in non-biological materials engineering, and was first developed for the study of rubber elasticity in the 1940's and 1950's by Treloar and Rivlin [30].

Lanir and Fung were the first to perform planar biaxial testing of soft biological tissues, specifically rabbit skin; they developed an optomechanical system capable of measuring two-dimensional mechanical properties, which consisted of a thermoregulated saline compartment, a stretching mechanism with force transducers and controllable sliding units, and a dimensional analysis system [31]. This system, and the tests conducted with it, demonstrated the basic mechanical properties of soft planar tissues: nonlinearity, repeatability after biaxial preconditioning, hysteresis, and weak dependence on strain-rate [32]. Technical improvements made since the above studies have allowed for the development of precise electronically-controlled systems for conducting planar biaxial mechanical tests, such as the Bose ElectroForce system that is used in our lab.

1.2.2 Constitutive Modeling

Soft biological tissues pose a challenge for simple material models due to their tendency to exhibit oriented fibrous structures, highly nonlinear stress-strain relationships, and viscoelastic properties. Tong and Fung developed a constitutive model for rabbit skin using the data collected in the experiment described above from Lanir and Fung [33]. They developed separate pseudo

strain-energy functions for both the loading and unloading phases of the preconditioned stress-strain curve, where the pseudo strain potential $\mathbf{W}(\mathbf{e_{ij}})$ is defined by the following relationship, where the in-plane second Piola-Kirchhoff stress components $\mathbf{S_{ij}}$ can be derived by differentiation:

$$\mathbf{S_{ij}} = \frac{\partial W}{\partial e_{ij}}$$

They assumed the tissue to be orthotropic, and expressed $\mathbf{W}$ with the following exponential function:

$$\begin{aligned}\mathbf{W} = &\frac{1}{2}(\alpha_1 e_1^2 + \alpha_2 e_2^2 + \alpha_3 e_{12}^2 + 2\alpha_4 e_1 e_2) \\ &+ \frac{1}{2} c \exp(a_1 e_1^2 + a_2 e_2^2 + a_3 e_{12}^2 + 2a_4 e_1 e_2 \\ &+ \gamma_1 e_1^3 + \gamma_2 e_2^3 + \gamma_4 e_1^2 e_2 + \gamma_5 e_1 e_2^2)\end{aligned}$$

An important distinction in this model is that, being a *pseudo* strain potential, it does not have the same thermodynamic meaning that the 'strain energy function' does due to its dependence on preconditioning, as well as the separation of loading and unloading. While this model was found to be effective in fitting the stress-strain data, it contains more parameters than are needed for a satisfactory fit, and can be reduced to the Fung-type function expressed and used in Section 7.3. Other constitutive models for describing soft biological tissues exist, but Fung's is the most broadly-used to date for many tissue types, including the myocardium [30].

1.3 Specific Aims

The goal of this project is to characterize the tissue-level mechanical properties of the right ventricle and its adaptation to pressure overload in pulmonary arterial hypertension. Since PAH is a disease more prevalent in women, but where pre-menopausal women present better survival outcomes, we propose to study the remodeling of the right ventricle in male and female rats using the well-established Sugen-Hypoxia animal model of PAH.

Aim 1: Investigate the mechanical properties of the right-ventricular free wall in male and female rats in a well-established animal model of PAH.

In a longitudinal study of PAH in male rats, Kwan *et al.* found the right ventricle to maintain cardiac function by increasing passive chamber stiffness. In their computational model of right ventricle organ-level mechanics, the sarcomere stress-length relation was stiffest in the SuHx week 8 group [14]. Since there was no up-regulation in contractile properties, we propose to validate those model predictions by mechanically testing RV free wall samples from female and male rats. We hypothesize that the passive properties of the RV myocardium wall increase with the disease progression, becoming stiffest at SuHx week 8, and later becoming more compliant, where female RV samples will be the more compliant at all stages. To test this, we will perform planar biaxial testing of intact myocardium at three stages of PAH progression: before, at, and after 8 weeks, and data will be fit to a Fung-type constitutive model for group averaging and comparison.

Aim 2: Investigate the mechanical properties of the collagen extracellular matrix.

Right-ventricular myocardium from male SuHx rats was previously found to be stiffer than the normotensive group in part due to the stiffening of the collagen ECM [15]. After 6 weeks of SuHx, Velez-Rendon *et al.* reported the RV ECM to be anisotropic, with the circumferential direction being the stiffest. Based on this, we hypothesize that collagen ECM remodeling in both male and female PAH will result in increased stresses in the diseased ECM, and that females

will stiffen less than males. To test this, we will perform planar biaxial testing of decellularized myocardium from male and female rats.

Chapter 2

Experimental Overview

The following sections will detail the experimental and analytical procedures carried out over the course of this project. To summarize briefly, PAH is first induced in male, female, and ovariectomized female rats via Sugen injection followed immediately by three weeks in chronic hypoxia (10% O_2). Following several weeks of disease development in normoxic conditions, the disease state is confirmed via invasive hemodynamic measurements recorded during terminal open-chest surgery. At the conclusion of this surgery, the right ventricle free wall is isolated and cut into a square to be used in biaxial testing, with tissue pieces removed from the edges of the square and saved for collagen quantification. The square of tissue is measured to determine the reference configuration, then subjected to quasi static biaxial testing. Following this mechanical testing, the tissue sample is decellularized, then the resulting square of extracellular matrix undergoes the same biaxial testing protocol. Data collected from the mechanical testing is processed and analyzed. Stress-strain curves are computed and fit to a Fung-type exponential strain-energy function. Strain-energy surfaces are generated to compute the mean and standard error from the mean to represent each group.

Chapter 3

Biological Considerations

3.1 PAH - Animal Model

In this study, we employ the SuHx rat model of PAH. This is a well-established animal model of PAH that involves the administration of Sugen, a vascular endothelial growth factor receptor antagonist, and chronic hypoxia exposure in rats. By combining these two factors, we achieve the formation of plexiform lesions and right-ventricular remodeling, which are characteristic features found in explant tissues of PAH patients. Here, intact female, male, and OVX female Sprague-Dawley rats (Charles River, Wilmington, MA) are randomly assigned to either the control or SuHx group. Male and female rats are ordered at approximately 6 and 7 weeks of age respectively, and all animals weigh approximately 200 grams at the time of Sugen injection. OVX females undergo ovariectomy at 6 weeks of age to remove their

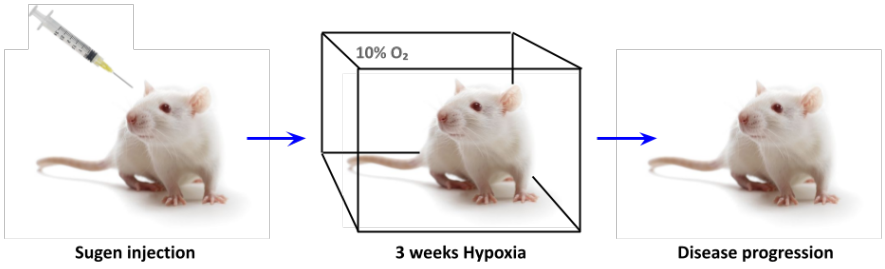

Figure 3.1. Schematic of the SuHx rat model for PAH. Sprague-Dawley rats are injected with Sugen, then exposed to chronic hypoxia for three weeks before removal to normoxia for additional weeks of disease progression.

ovaries. At the time of their arrival to UC San Diego, all SuHx-assigned rats are administered a single subcutaneous injection (20 mg/kg) of Sugen on the posterior of the neck. Injectable Sugen is prepared by dissolving 25 mg powdered Sugen (SU5416, S8442 MilliporeSigma, CAS Number 204005-46-9, PubChem Substance ID 24278606 Sigma-Aldrich, MO) in 1.25 mL dimethysulfoxide (DMSO). The thoroughly mixed solution is filtered through a 0.2 um syringe filter prior to administration and stored at -20°C if not immediately used. Following the injection, the rats are exposed to chronic hypoxia (10% O_2) for three weeks, after which they are returned to normoxic conditions. Week 3 SuHx animals undergo the terminal data-acquisition and tissue harvesting procedure the day of removal from hypoxia, and later-week animals remain in normoxia for the remainder of disease progression, up to Week 15 (12 weeks normoxia). Age-matched control animals are kept in normoxia throughout the entirety of the study.

3.2 Invasive Hemodynamic Measurements

To obtain hemodynamic measurements and confirm PAH in the animal, terminal open-chest surgery is performed. A mPAP above 20 mmHg serves as an indicator of the disease state. Initially, the animal is weighed and then placed in an induction chamber supplied with 5% isoflurane (MWI Veterinary Supply, Cat. No. 502017) until unconsciousness is achieved, which is verified by toe pinch. Subsequently, the rat is transferred to the surgery platform and connected to a nose cone, through which it continuously receives anesthesia consisting of oxygen mixed with 2.5% isoflurane. To monitor temperature, a rectal probe (MicroTherma 2, ThermoWorks, UT) is inserted, and electrodes for a 4-lead electrocardiogram are placed on each limb to monitor heart rate. The rat undergoes tracheotomy and is intubated using the E-Z Anesthesia Ventilation System (Palmer, PA, USA), with the breathing rate set at 50 breaths/minute and tidal volume adjusted based on the rat's weight.

A thoracotomy is performed to expose the heart, lungs, and major vessels. After removing the pericardium, a 25-gauge needle is inserted apically into the right ventricle and immediately

replaced by a 1.9-French admittance catheter (Transonic Scisense, ON, Canada). Once the pressure-volume (P-V) time series are recorded, steady-state measurements are followed by occlusion of the inferior vena cava to record changes in preload. The recorded P-V loops are later averaged for cardiac function analysis. A second incision is then made on the outflow tract to insert a dual pressure catheter, that goes past the pulmonary valve to measure pulmonary arterial pressure. Mean pulmonary arterial pressure is calculated by summing two-thirds of end-diastolic pressure with one-third end-systolic pressure. The surgical procedure ends with the increase to 5% isoflurane, exsanguination of the animal, and flush of ice-cold phosphate-buffered saline (pH of 7.4) with heparin. The right-ventricle is immediately isolated and prepared for mechanical testing.

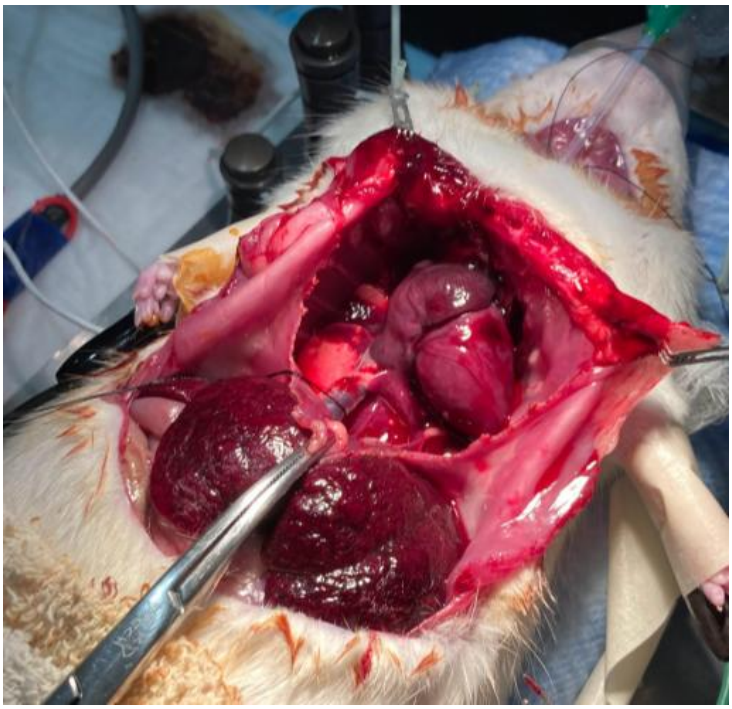

Figure 3.2. Open-chest procedure in a PAH rat exposing the heart, lungs, and major vessels. Note the enlarged right atria and granular appearance of the liver due to the disease.

3.3 Decellularization

To determine the contribution of the collagen ECM, we chemically decellularize the sample of RV myocardium. This process removes the cells from the tissue sample after being mechanically tested. While maintaining the markers on the epicardium of the sample, the now collagen-ECM is mechanically tested.

Decellularization is performed by placing the square samples of RV free wall (these have already been prepared and tested as described below – see Sections 5.1 and 5.2) individually in cell strainers that are submersed in a solution of 0.5% sodium dodecyl sulfate (SDS) in 10 mM Tris-buffered saline and left on a stir plate at room temperature for 24 hours. SDS is a strong ionic detergent that acts to denature the proteins and solubilize cellular and nucleic membranes. This solution is replaced every 24 hours until the tissue samples appear colorless and transparent, indicating complete decellularization (Figure 3.3). Typical duration of SDS soak is 3-5 days, but can take longer depending on the thickness of the tissue, as thicker samples require more time for the cells to be fully removed from the center of the piece. Following completion of decellularization in SDS, the tissues are transferred to a 24-hour wash in 0.1 M phenylmethylsulfonyl fluoride (PMSF) in 1x phosphate-buffered saline (PBS) solution, again on a stir plate at room temperature. PMSF is a serine protease inhibitor that halts the decellularization process and protects the tissues from further damage and degradation. Once the PMSF wash is complete, the tissues are removed to petri dishes where they are submerged in pH 7.4 PBS and kept in 4°C refrigeration until the time of decellularized mechanical testing.

3.4 Collagen Content

To quantify the amount of collagen present in the RV samples, we perform collagen assays on pieces taken from various sections of the RV free wall. Aiming to quantify changes not only with the disease state and between sexes, but also spatially within samples, these experiments provide information about the composition of the ventricle, which has been consistently observed

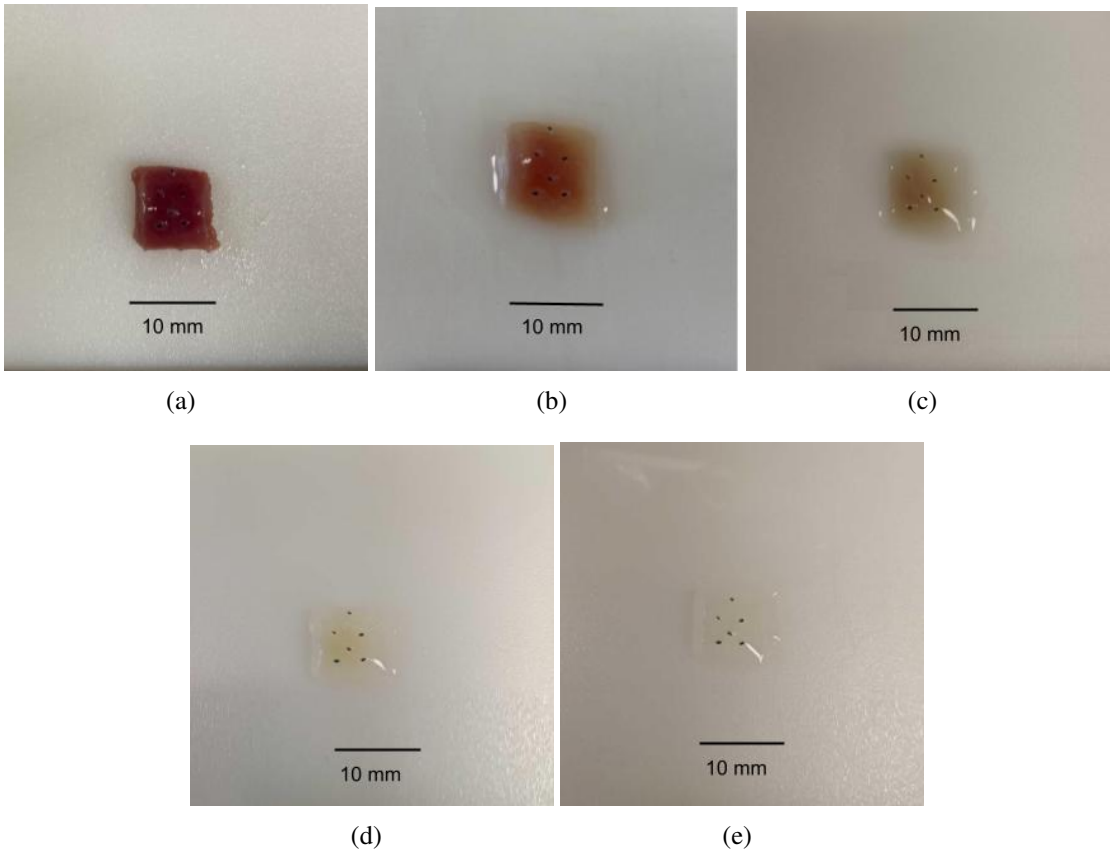

Figure 3.3. Progression of the decellularization process in an RV tissue sample. Tissue after: (a) zero days in SDS (day of mechanical testing); (b) one day in SDS; (c) two days in SDS; (d) three days in SDS; and (e) seven days in SDS.

(during tissue preparation as described in Section 5.1) to have spatial heterogeneity in thickness. The left side of the tissue square (denoting the outflow edge as the top) consistently has greater thickness than the right side, and this difference is more pronounced in SuHx animals. Findings from these experiments can be used in conjunction with mechanical properties observed during biaxial testing experiments to help better understand the role of collagen in the mechanical remodeling that occurs during PAH, and how it might differ between sexes and spatially within the ventricle. Perhaps even later studies may attempt to link these differences to mechanisms of RV hypertrophy and hemodynamic changes.

3.4.1 Tissue collection

RV samples harvested as of March 2023 underwent additional steps during the tissue preparation protocol described in Section 5.1 whereby, when the excised right ventricle is obtained, it is first cut into a larger square than will be used for biaxial testing, and small pieces from each edge of the square (top-outflow, bottom-apex, left, and right) are carefully sliced off and placed in individual tubes for later use in collagen assays (Figure 5.2). These samples are flash frozen and stored in -80°C until the day that the collagen assay procedure is initiated.

3.4.2 Collagen assay procedure

Frozen samples of RV tissue are gently blotted dry with absorbent tissue, then the mass is measured and the pieces are placed in tubes where they will undergo steps from the Sensitive Tissue Collagen Assay (QuickZyme Biosciences, Netherlands). This assay detects hydroxyproline, a non-proteinogenic amino acid that can function as a direct measurement of the amount of total collagen in a tissue sample, with no distinction between the different types of collagen. Briefly, the tissue is completely hydrolyzed in 6M HCl at 95°C for 20 hours, after which the samples are centrifuged and the supernatant is removed and diluted. The hydrolyzed and diluted samples are then pipetted to a 96-well assay microplate, where an assay buffer and enhancer solution are added before 20 minutes of incubation and shaking at room temperature. Subsequently, a detection reagent solution is added, and the plate is again incubated while shaking, this time for 22 minutes at 60°C. Upon completion of this step, the colors in the wells have changed to reflect the concentration of collagen in the solution (Figure 3.4). Finally, the plate is cooled on ice for 5 minutes before insertion into the Tecan microplate reader (Tecan LifeSciences, CH), where absorbance is measured at a wavelength of 560 nm.

3.4.3 Analysis - Collagen quantification

The scanner records 12 readings from each well of the assay plate. Our data showed abnormalities in 4 of these 12 readings, where the absorbance was reported to be higher than

Figure 3.4. A 96-well plate after completion of the collagen assay protocol. This is inserted into the scanner for optical quantification of total collagen content, where a darker red in the well indicates higher collagen content.

other readings. After testing to confirm that this was a malfunction of the plate reader and not the collagen wells, the outliers were removed, leaving 8 usable readings per well. These readings are used to calculate the mean absorbance for each well, which is then averaged with the duplicate well from the same tissue sample. A linear fit from the collagen standard data is then used to convert the averaged absorbance into collagen concentration [ug/mL], which can then be converted to total collagen [ug] by multiplying with the fluid volume, and finally to collagen per tissue weight [ug/mg] by dividing by the mass of the tissue sample used. This results in a value of total collagen normalized by tissue weight for each sample tested, which can then be further averaged for comparisons of sex, treatment, or region.

Chapter 4

Technical Considerations

In this study, as in all others, many assumptions and considerations were taken. This section will discuss experimental assumptions and limitations due to instrumentation.

4.1 Biaxial Testing Assumptions

Biaxial testing of the myocardium assumes in-plane forces and deformations, considering the third dimension minimal. Therefore, it is important for our experimental set up to be fully in-plane and have no vertical changes. This is accomplished by use of the pulley system (Figure 4.1), which is assumed to be friction-free and allows for the tissue to move freely in the desired two dimensions, enabling us to neglect shear stresses. Additionally, the sutures themselves are assumed to remain unstretched during the loading and unloading cycles, ensuring that the linear displacement from the movers is fully applied to the tissue's edge. The hooks used to apply this displacement at the tissue's edge are considered to have negligible boundary conditions within the region of strain observation. Furthermore, it is assumed that the force applied by the hooks acts uniformly across the entire cross-sectional area of the tissue.

Although the cross-sectional area is computed using an average of five thickness values, we assume the tissue to have uniform thickness and to be incompressible. Moreover, the thickness of the tissue wall is considered thin compared to other dimensions, consistent with the assumptions of a thin-walled ventricular model. This implies that stresses act solely in the two

perpendicular directions within the plane of the surface, and these stresses are assumed to be uniform across the thickness of the wall [34].

During the testing in the bath, we assume that the tissue is sufficiently preloaded to ensure that the stretch it undergoes remains within the plane of the tissue. This includes consideration of the added mass from the hooks, which can sink the tissue out of the plane of the movers if too heavy. Furthermore, when selecting loading cycles for averaging and modeling during data analysis, we assume that the tissue has undergone sufficient preconditioning to ensure the repeatability of cycles.

4.2 Reference Configurations and Tissue State Definitions

To accurately describe the stresses and strains experienced by the RV sample in this experiment, it is necessary to establish consistent reference states or configurations. In this study, we focus on characterizing the passive mechanical properties of the RV myocardium, which would correspond to the unloaded state or at end-diastole. However, in this physiological state, the RV would be adhered to the left ventricle, which is not representative of our experimental setup. Therefore, we consider the unloaded zero-stress state β_0 instead when the RV is detached from the septum and left ventricle and flattened on a cutting board right before the length, width, and thickness are measured. These dimension measurements in the undeformed state will serve as the Lagrangian reference in our stress calculations.

Between the unloaded and deformed/stretched tissue states, we establish a tare-loaded configuration denoted as β_1. This configuration serves as the reference state for strain calculations. It represents the tissue state in which a predetermined load (3.0 grams) is applied to ensure consistency across samples and trials. However, to align with the unloaded reference state for stress analysis, it is crucial to establish a mapping between β_1 and β_0, as explained in Section 5.7.2.

In practice, the same tare-loaded reference configuration is not used throughout the

duration of the experiment since the load cells tend to drift over the course of the trial. As such, a unique reference configuration is used for each block of the stretch protocol. Before this change was implemented, the foot of each stress-strain curve would drift with the load cells, resulting in five averaged-loops that do not all begin/end at zero strain. Now, the block-specific reference configuration is defined at the beginning of the third-to-last loading-unloading cycle, the first of the data that are used for averaging, and the resulting loops are generally neater and better for modelling.

Finally, the current or deformed configuration (β_2) refers to the state where real-time measurements of load and displacement are recorded during the experiment. This configuration represents the instantaneous state of the tissue as it undergoes stretching from its tare-loaded state and subsequently returns to that state in each loading-unloading cycle.

4.3 Bioinstrumentation

4.3.1 Mechanical bioinstrumentation

The Bose planar biaxial testbench system (Figure 4.1) delivers precise displacement-controlled stretches via four ElectroForce friction-free moving-magnet linear motors. These operate by applying an electrical current through a coil, which induces a magnetic field that then attracts or repels the magnetic actuator, generating a force proportional to the current. Through precise calibration, this enables measurement and control of edge displacements (displacement applied at the edge of the tissue sample).

The two axial loads are measured by load cells mounted to the arms of the two movers which control the two perpendicular axes. The load cell measures load in grams by applying and reading voltage changes across a Wheatstone bridge circuit, in which there is embedded a strain gauge that experiences changes in resistance under applied strain. Changes in voltage are calibrated to known applied loads, and thus allow for continuous measurement and calculation of load applied to the tissue.

While edge displacement is measured by the movers, we are interested in studying the small strains that occur near the center of the tissue, so a pixel-tracking camera system is used to capture and record marker locations for strain calculations, described later in Section 7.2. The camera used is the Prosilica GE680, and the software used is the Vision 4.2 2D Marker Tracking video extensometer. It records the pixel positions of five markers placed on the surface of the tissue sample, with a sampling frequency of 200 Hz. The system interface requires manual adjustment of threshold (to produce a binary image defined by the appropriate intensity to capture markers) and marker size (to track regions large enough to contain each marker without unnecessary risk of tracking unwanted objects in the bath).

There are some experimental limitations to the instruments described above. One is that the load cells are extremely temperature-dependent and generally noisy, which results in sometimes significant drift. The effects of this are minimized by regular taring of the load cells during mechanical testing, as well as use of block-unique reference configurations (see Sections 5 and 4.2 for further detail), but it remains a limitation that should be taken into consideration. An additional limitation is interference of visual obstructions that can corrupt marker-tracking in the camera system. When an external object such as a piece of dust or bubble floating on the surface of the fluid in the test bath crosses between the camera and the markers it is tracking, it can disrupt the signal, resulting in faulty strain calculations or early termination of the test. We attempt to avoid this by manually removing any visible debris from the test fluid, but it poses a challenge that is at times unavoidable and can only be mitigated by restarting the test.

4.3.2 Hemodynamic bioinstrumentation

Pressure and volume *in vivo* hemodynamic measurements taken during open-chest surgery are measured by two different catheters: a Pressure-Volume (PV) catheter, which has both a pressure and a volume sensor, and a Dual-Pressure (DP) catheter, which has two pressure sensors. The pressure sensor (a piezoresistive strain gauge) consists of a deformable membrane with a thin circuit, which deforms and changes resistance when the catheter experiences pressure

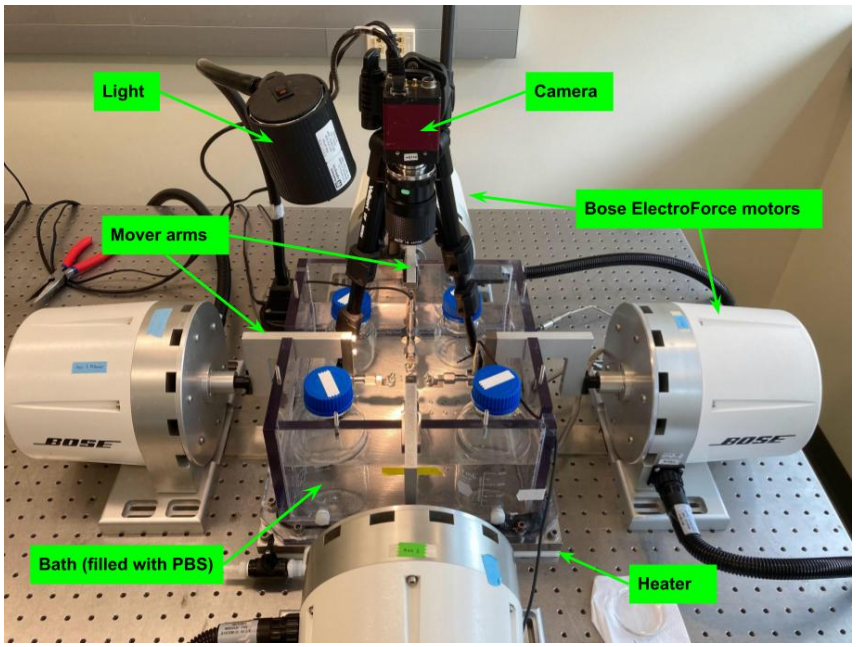

(a)

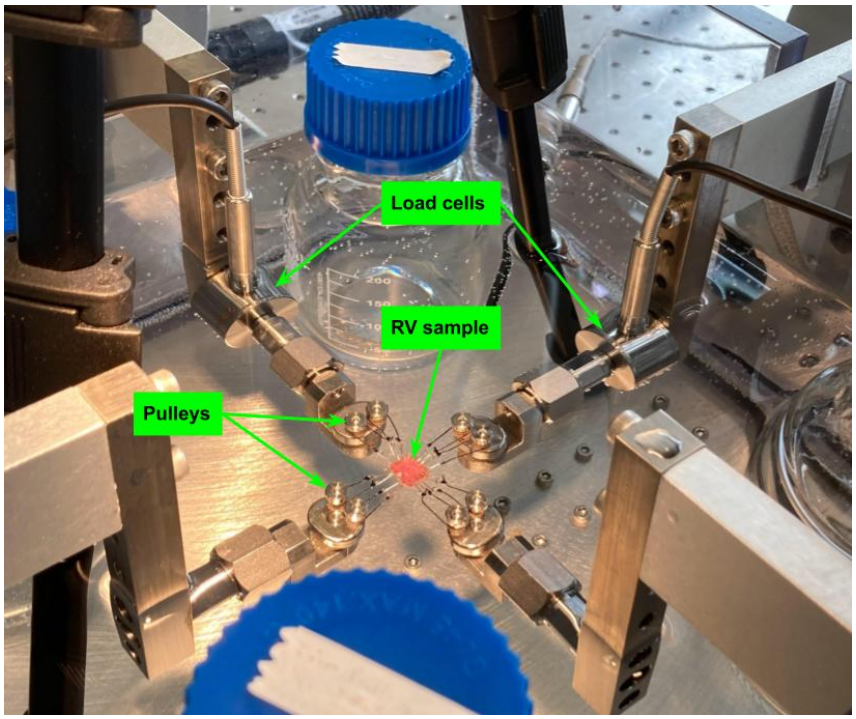

(b)

Figure 4.1. Annotated images of (a) table-view and (b) closer-in bath-view of the Bose test bench setup.

changes. Resistance changes across the Wheatstone bridge circuit result in an output voltage that communicates instantaneous strain values to the computer, which can be calibrated to translate voltage to pressure readings. The volume sensor measures electrical fields to compute chamber volume of the heart. Blood within the chamber has resistive properties, and the cardiac muscle of the chamber has both resistive and capacitive properties, so by use of electrical admittance theory this allows for continuous measurement of the blood and muscle, who's contributions can be separated to calculate an approximate measure of ventricular volume.

Flow through the pulmonary artery is measured by a transit-time ultrasonic flowmeter. This device is placed around the external wall of the pulmonary artery, where two ultrasonic transducers on one side of the probe send and receive signals that are passed through the bloodstream and reflected back by a fixed acoustic reflector on the other side of the probe. By measuring the distance in time it takes the signal to be transmitted from one transducer and reflected to the other, the volume flow can be computed.

4.4 Hook-making Protocol

To ensure a fully planar biaxial text, the sample assembled onto the testing device needs align with the linear actuators to avoid motion in the vertical direction. To this end, several considerations are taken into account. First, the sutures need not be worn down to the point of lost integrity, i.e. they cannot be old and overused, else they will become stretchy and hence fail to appropriately stretch the tissue. Second, the hooks need be small enough as to not weigh the tissue down, for excessively large hooks are heavy and cause the tissue to sink in the bath. Third, the lengths of the hook-suture pairs needs to be consistent from one pair to the next within a set of hooks This ensures that the tissue is being stretched equally across each side, for if one hook was longer than its neighbor, the tissue would be held and stretched at a skewed angle in the bath. The pulleys that support the sutures provide some rotation to help mitigate this constraint, but care should be taken nonetheless to ensure the hooks are manufactured with the highest precision

humanly possible.

Therefore, custom hooks are made in-lab for use in tissue setup for the planar biaxial testing according to the following protocol, documented by Jessica Huberts and Becky Hardie to promote consistency in the hook-making process.

Materials:

- 0.012 soft stainless steel rods
- Size 3-0 USP (2.0 metric) braided silk suture line
- Glue

Tools:

- Dremel with heavy-duty cut-off wheel attachment (No.420)
- Metal clippers
- Small scissors
- Forceps
- Hemostats

Instructions:

1. Cut metal rods into small pieces ($\approx$ 25mm, depending on maker preference) using metal clippers.
2. Use dremel to sharpen one end of metal piece to a needle-like point.
3. Bend the piece into hook shape using hemostat and forceps. Hook size will depend on the need (small/large, customized to fit various tissue thicknesses). See existing hooks for reference/comparison.

   Note: *Main constraint: the hook needs to be big and strong enough to secure tissue without adding excessive weight and pulling the sample down.*

4. Assess size of hooks to match pairs, so pairs are as equal in size as possible. For a complete set, you need 16 hooks total (8 pairs).

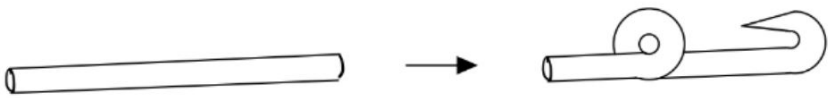

Figure 4.2. Hook-making protocol, Steps 1-3: the metal rod should be cut, sharpened, and bent at both ends to form a hook with a loop for tying.

5. Use scissors to cut a small length of suture line, and tie one hook from each pair to one end of the suture. Then carefully tie the second hook to the other end, making sure that the *length from the end of one hook to the end of the other* is consistent from pair to pair (Figure 4.3).

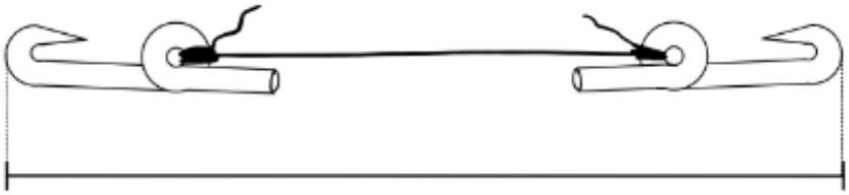

Figure 4.3. Hook-making protocol Step 5: the end-end length of hook-suture pairs should be consistent.

6. Apply a small drop of glue to each knot of suture and let dry overnight.
7. Use scissors to trim excess suture lines and clippers to trim excess metal.

Chapter 5

Mechanical Testing

5.1 Right-Ventricular Tissue Preparation

After open-chest surgery and hemodynamic measurements are completed, the right ventricle tissue must be prepared for mechanical testing in a meticulous and consistent manner in order to ensure that experimental data is reliable. The sample of rat right-ventricular myocardium is excised from the animal (Figure 5.1) and cut via razor blade into a square in which one axis is aligned with the apex to outflow (AOT) direction (x_1), and the other with the perpendicular circumferential direction (x_2) (Figure 5.2). The directions are determined by identifying the outflow valve (typically visible as a thin, whitish flap-like structure) at one end of the free wall, and the apex at the other end (the apex typically has a visible blood clot or puncture wound visible from where the catheter was previously inserted). The side lengths of the square are measured with a digital caliper, and five thickness measurements are recorded from various locations using both a digital caliper and a dial caliper in order to calculate the average tissue thickness. The outflow edge of the tissue is labeled with a graphite marker, and five additional markers are placed to form a center-marked square near the center of the tissue to track deformation (Figure 5.3). Four custom-made hooks are inserted through each side of the sample, and sutures tied to the hook ends are used to load the sample onto the Bose ElectroForce planar biaxial testing device, in which the tissue is fully submerged in a bath of phosphate-buffered saline, kept at 36.5°Celsius and with pH 7.4.

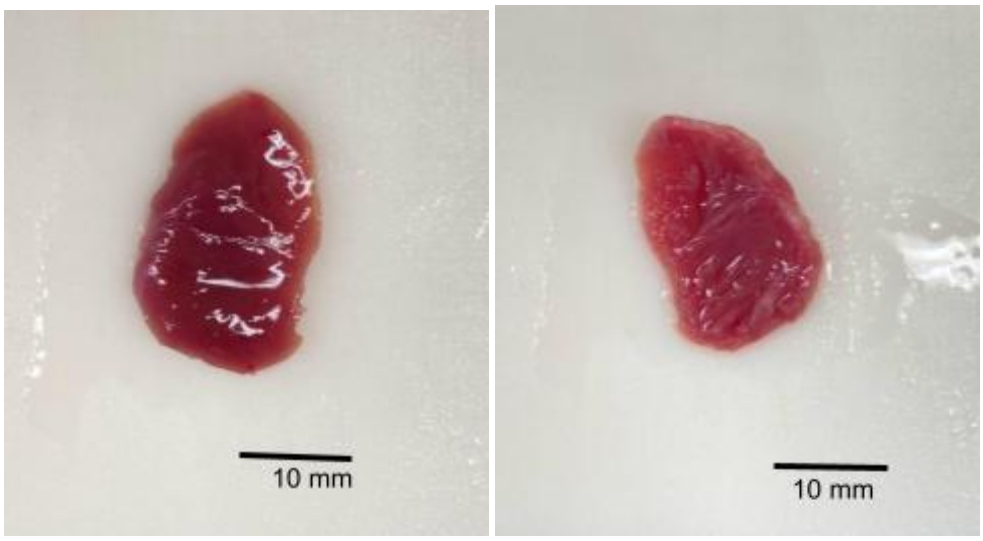

(a) (b)

Figure 5.1. Right-ventricular free wall isolated from the heart. Epicardium (a) of the myocardium is where the markers are placed to track deformation, and the inner or endocardium (b) of the myocardium.

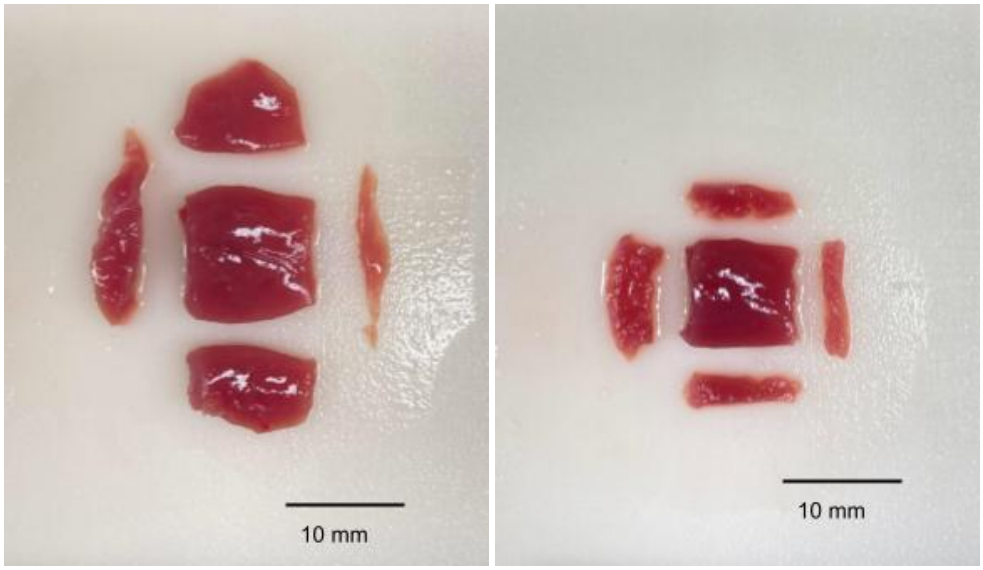

(a) (b)

Figure 5.2. (a) The excised RV is first cut into a square by making cuts along the four sides. (b) Then slices of tissue are removed from the edges of the square and saved for collagen assays. This image shows a significant difference in thickness when comparing the slices removed from the left and right sides of the square.

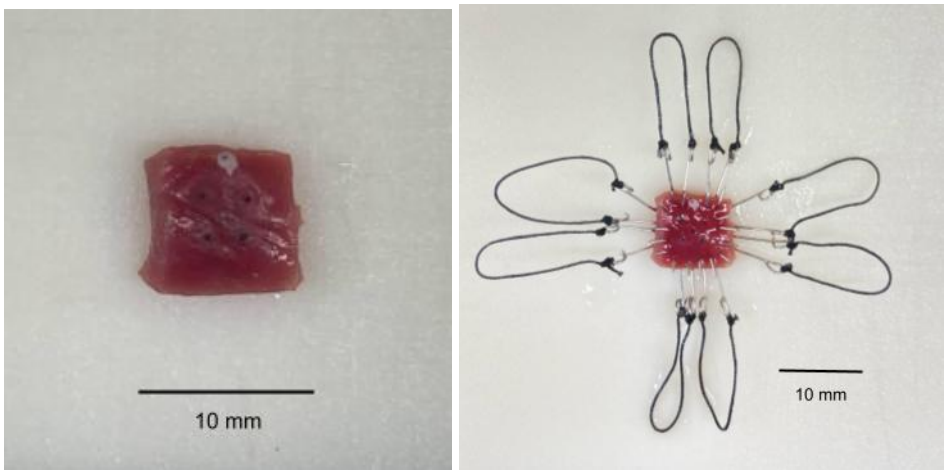

(a) (b)

Figure 5.3. (a) Five markers are placed near the center of the square, and one marker is placed at the outflow edge (top). (b) Four hooks are inserted through each side of the tissue, attached to suture loops.

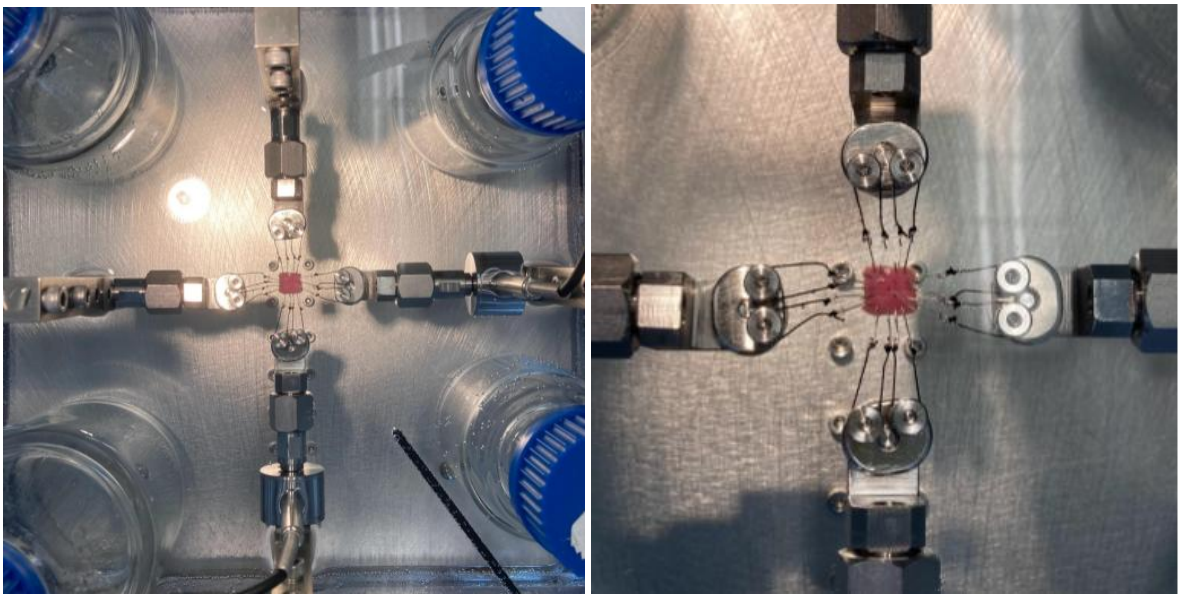

(a) (b)

Figure 5.4. An example of a RV sample loaded into the test bath. (a) Four jars of tap water are used to fill volume, requiring less PBS in the bath. (b) Each suture is looped around a pulley that can rotate freely, allowing the tissue to remain straight and centered.

5.2 Intact Myocardium

Once secured in the bath, the sample is pre-stretched to a load of 3.0 grams, ensuring that the tissue is pulled upwards into the plane of the movers and starts from a consistent reference (Figure 5.4), and subsequently subjected to a displacement-controlled biaxial testing protocol, consisting of seven blocks, each with 15 triangle-waveform loading-unloading cycles performed at 0.5 Hz. The $x_1 : x_2$ stretch ratios in each of the seven blocks are 1:1, 1:0.5, 1:0.25, 1:1, 0.5:1, 0.25:1, and 1:1, with a maximum stretch of either 8% (Table 5.1) or 10% (Table 5.2) of the *ex vivo* length. This protocol is run ideally four to five times, first at 8% then at 10%, with additionally trials run as needed depending on the success of the trials and the quality/resilience of the tissue sample; between each trial of the protocol, the tissue is manually unloaded and the load cells are tared to minimize the effects of the drift.

A recent addition to the protocol was implemented in June 2022 whereby, before the initiation of recorded loading and unloading cycles, a set of preconditioning stretches is applied, which equibiaxally stretches the tissue once to 8%, once to 10%, and once to 12% of *ex vivo* length at a rate of 0.2 Hz, again with triangle waveforms. This entire preconditioning stretch series is repeated twice, with the load cells tared before each, and serves the purpose of straightening the hooks in the tissue, aligning the suture lines with the pulley system of the movers, and providing some preconditioning of the tissue itself.

After mechanical testing is complete, the side lengths and thickness of the intact tissue are measured once more with the digital caliper, and the tissue is transferred for decellularization as described in Section 3.3.

5.3 Decellularized Myocardium

The decellularization process described in Section 3.3 ends with a square sample of ECM tissue that was previously subjected to mechanical testing as an intact sample. The decellularized tissue usually retains its markers from the previous test, but if not, any missing markers are

Table 5.1. Stretch ratios used in the seven blocks of the 8% stretch protocol, applied at 0.5 Hz. The first half of the test stretches Axis 1 at 8% while Axis 2 is varied at smaller stretch levels, and the second half of the test does the opposite, with Blocks 1, 4, and 7 each being equibiaxial stretch blocks. This stretch protocol is run before 10%, and aims to capture stretch values that are more directly comparable to those from shrunken decellularized tissues.

Block	Axis 1 Stretch	Axis 2 Stretch
1	8%	8%
2	8%	4%
3	4%	2%
4	8%	8%
5	4%	8%
6	2%	8%
7	8%	8%

Table 5.2. Stretch ratios used in the seven blocks of the 10% stretch protocol, applied at 0.5 Hz. The first half of the test stretches Axis 1 at 10% while Axis 2 is varied at smaller stretch levels, and the second half of the test does the opposite, with Blocks 1, 4, and 7 each being equibiaxial stretch blocks. This is the stretch protocol most commonly used in modelling analysis.

Block	Axis 1 Stretch	Axis 2 Stretch
1	10%	10%
2	10%	5%
3	10%	2.5%
4	10%	10%
5	5%	10%
6	2.5%	10%
7	10%	10%

reapplied, and the sample is gently blotted dry with absorbent tissue in order to accurately measure its side lengths. In order to avoid squishing the delicate tissue, thickness measurements are not taken with a digital caliper, but instead with a laser micrometer, where similar to intact tissue preparation, five measurements are used to compute an average thickness. Since the tissue must be placed on a custom-made table stand to be measured using the laser, the thickness of the stand is measured and subtracted from the five recorded measurements. Again, four custom-made hooks are inserted through the sides of the sample, and sutures are used to load the sample into the Bose testing device, where this time the decellularized tissue is submerged in room-temperature phosphate-buffered saline, pH 7.4.

The mechanical testing protocol for decellularized tissues mirrors that of intact tissues, with some minor alterations. Being smaller, lighter, and more delicate, the decellularized tissues are pre-stretched to a load of 0.8 grams (rather than 3.0 grams like intact tissues). The same protocol of 8%, 10%, 12% at 0.2 Hz preconditioning stretch is applied, then the 10% stretch protocol in Table 5.2 is enacted. The tissue is again manually unloaded and the load cells tared between each trial. Following successful recording of at least one 10% stretch trial, decellularized tissues are subjected to additional trials at 12% stretch, as detailed in Table 5.3.

After completion of all mechanical testing, the decellularized tissue is removed from the bath and side lengths are again measured via digital caliper, then thickness is measured by laser and again by caliper. Finally, mass is recorded and the tissue is transferred into a petri dish of neutral buffered formalin for fixation. After 48 hours in formalin, the fixed tissue is removed to a tube of 70% ethanol where it can be stored in a cupboard for any later uses such as imaging.

Table 5.3. Stretch ratios used in the seven blocks of the 12% stretch protocol, applied at 0.5 Hz. The first half of the test stretches Axis 1 at 12% while Axis 2 is varied at smaller stretch levels, and the second half of the test does the opposite, with Blocks 1, 4, and 7 each being equibiaxial stretch blocks. This stretch protocol is only applied to decellularized tissue samples, after 10% stretch has already been recorded.

Block	Axis 1 Stretch	Axis 2 Stretch
1	12%	12%
2	12%	6%
3	12%	3%
4	12%	12%
5	6%	12%
6	3%	12%
7	12%	12%

Chapter 6

Data Processing

6.1 Data Acquisition

Five files of raw data are recorded and saved for each test that is run. Four of these files are from the Bose planar biax system and contain information from the load cells and motor controls, and one is from the camera and contains pixel positions of the five markers. Only the camera file and one of the four biax files are used: it is a ".txt" file that includes both test-recorded and self-referential data in a comma-separated table, where each row contains data recorded at a single time point. We extract three columns of data from this file: Load 1, Load 2, and Disp 4. Loads 1 and 2 are the loads measured by the two load cells in axis 1 and axis 2, respectively; these measurements have already been converted from a voltage to a load (in grams) by the experimental software. Disp 4 is the displacement from Motor 4, and is only used as an alignment signal, which will be described below. Biax data is sampled at 20 Hz.

The camera file, like the biax file, contains data organized in a comma-separated table with each row representing a time point. Columns contain x- and y- pixel coordinate values for each of the five tracked markers, as well as some additional automatically-calculated values that we do not use (it computes strain using a different reference configuration than we do, and is thus not useful to us except for aligning data). As previously mentioned, camera data is sampled at 200 Hz.

In addition to these data that are generated by the test systems, data recorded manually

during the experiment is input in a “Biaxial Geometry Database” spreadsheet. This spreadsheet contains side length and thickness measurements that are used in the following processing and calculations, as well as a record of which trial(s) worked for each animal, and if they are usable for analysis.

6.2 Data Pre-processing

The primary analysis code consists of three main functions that ultimately convert the raw test data described above to smoothed and averaged stress vs strain data, which can be used in later steps for model fitting. These functions are run in Google Colab, and automatically retrieve files from the lab Google Drive.

The first portion of this code is called AlignData, and as the name suggests, it functions as the initial processing step to convert the raw output data files into usable pre-processed data in which the load and camera outputs are aligned, as well as resampled to the same sampling frequency and cropped to remove portions of the trial that are not used for further analysis. It does this by first extracting the relevant columns of data from the given input files, then cropping a designated amount of data from the beginning and/or end of the extracted columns. This cropped amount is designated by the user in a block of code titled “Possible Corrections”, where the user must visually assess the alignment of the signals and manually type a number (in seconds) of data which will be removed in order to ensure the first peak of the Disp 4 data from the biax is lined up with the first peak of one of the pre-calculated value columns from the camera.

An alignsignals function is used to align the camera and biax data by finding the delay between the two, then padding the early signal and truncating the late signal so they are returned as the same length. It finds the delay using a finddelay function, which estimates the delay by either using the time shift from the signal cross-correlation, or by finding the distance between corresponding peaks.

A resample function is used to convert the 20 Hz data from the biax system to match

the camera data at 200 Hz using a cubic interpolation. The index where the peaks drop for the first time is used to identify the end of the first stretch block, and data before this point is removed so that the file now begins at the trough which marks the start of the second stretch block. Three figures are generated in this portion of the code: Raw Data Loops showing Load [g] *vs* Displacement [mm] (Figure 6.1), Aligned Data showing matched peaks from the biax and camera, and a zoomed-out plot of peaks showing the cropped blocks (Figure 6.2). Finally, the camera data is smoothed using a Savitzky-Golay filter (sub-sets of adjacent data are fit with a polynomial function using a linear least-squares method) and the data is saved to a "_PrePdata.txt" file with the following matrix columns: time [s], Load1 [g], Load2 [g], X1, Y1, X2, Y2, X3, Y3, X4, and Y4.

6.3 Data Processing

The next portion of the primary analysis code is called Kinematics. This code receives the aligned load and pixel data and from it calculates stress and strain for the entirety of the test. It also extracts the tissue dimensions from the geometry database and uses them to calculate the cross-sectional area, by which the loads – after conversion from grams to Newtons – are divided to obtain the Nominal stress tensor. The code then performs isoparametric mapping to calculate the deformation gradient tensor from the pixel positions. The calculations are described in Section 7.2.1, and are implemented using Python matrix operations. As detailed in the further subsection on stress and strain calculations, this deformation gradient tensor is also used to calculate the Cauchy-Green deformation tensor, which is then used to calculate the Lagrangian-Green strain tensor. The final task of the Kinematics code is to calculate the 2nd Piola-Kirchhoff (PK2) stress tensor using the Nominal stress (which is equivalent to the 1st Piola-Kirchhoff stress due to its diagonal nature) and the deformation gradient tensor. Again, these calculations are detailed below. Before saving the relevant data computed in this block of code, the axial stresses are smoothed and compiled as columns of a matrix, along with the strains.

Kinematics also generates and saves figures for the pixel locations (Figure 6.3), loads versus time (Figure 6.4), components of the deformation gradient tensor (Figure 6.5), Green-Lagrangian strain tensor with the normal strains E_{11} and E_{22} plotted against one another (Figure 6.6), and 2nd Piola-Kirchhoff stress tensor versus time, (Figure 6.7). These figures are checked by the user for analysis errors before running the final section of primary analysis.

The final section of primary analysis is called "CycleSelection", which receives the stress-strain data from Kinematics and identifies and isolates the last three stretch cycles from each block for averaging and strain energy calculation. It identifies the stretch cycles using the axis 1 stress vector for detection of peaks and troughs, the same way it is done in Kinematics. The peaks and troughs are used to then extract list data from the last three stretch cycles and compile them in 3D nested lists containing "full cycles" (data between two sequential troughs, both loading and unloading), loading curves (data between a trough and the next following peak), and unloading curves (data between a peak and the next following trough). A plot is generated for stress versus time (Figure 6.8), with circles and plus sign markers placed at the troughs and peaks of the three chosen cycles, as well as a plot of stress versus strain for the same three loops (Figure 6.9). Then averaged curves are calculated for each stretch block by taking a point-wise average of the three chosen cycles, and accumulated energy is calculated by taking a cumulative trapezoidal integral of the stress over strain. Plots are created for both of these (Figure 6.10), and the data arrays for each block combined and rearranged to form a single matrix with the following data columns: $E_{11}, E_{22}, S_{11}, S_{22}, W$ (where W is the accumulated strain energy). The last plot generated and saved in the primary analysis code shows data points for the averaged loading curves (Figure 6.11).

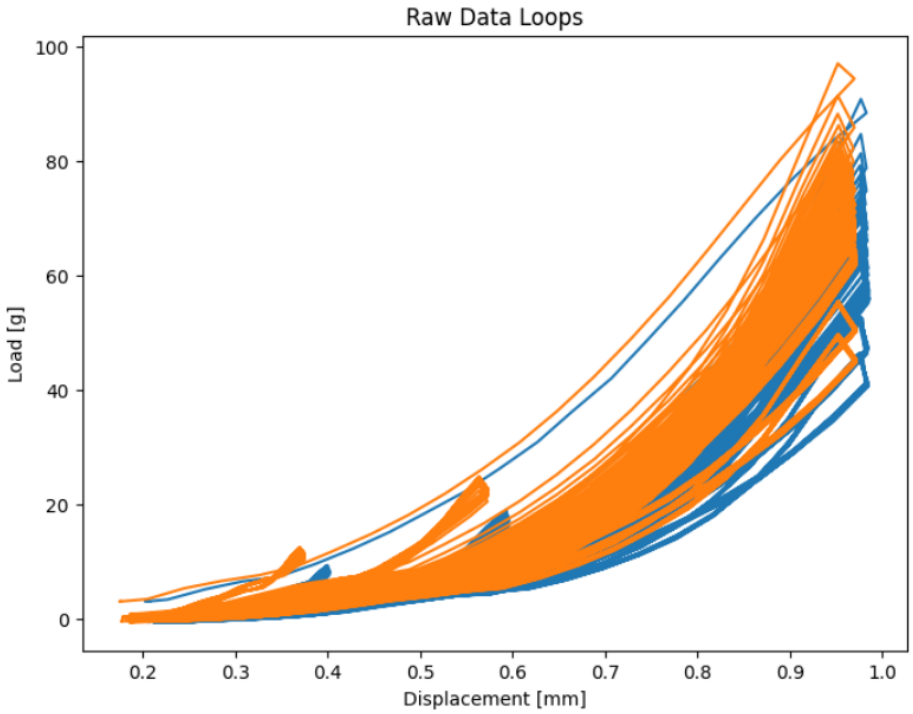

Figure 6.1. Illustration of the loading-unloading curves of the displacement measured from the actuators. The data includes 105 loading-unloading cycles from a typical stretch protocol, including both those used for averaging and the preconditioning loops that come before them. Data is from female SuHx Rat number 170, Trial 3.

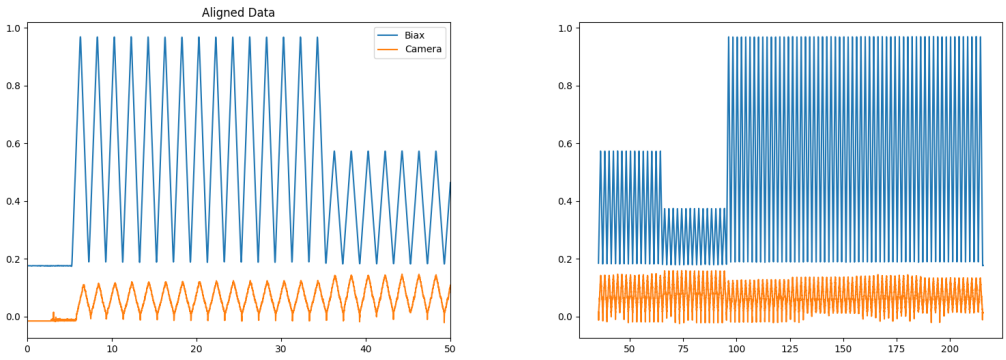

(a) (b)

Figure 6.2. (a) An example of Aligned Data and (b) All Data plotted for Female SuHx Rat 170 Trial 3. Note that the orange and blue peaks are lined up to occur at the same time point, indicating that the data has been properly aligned.

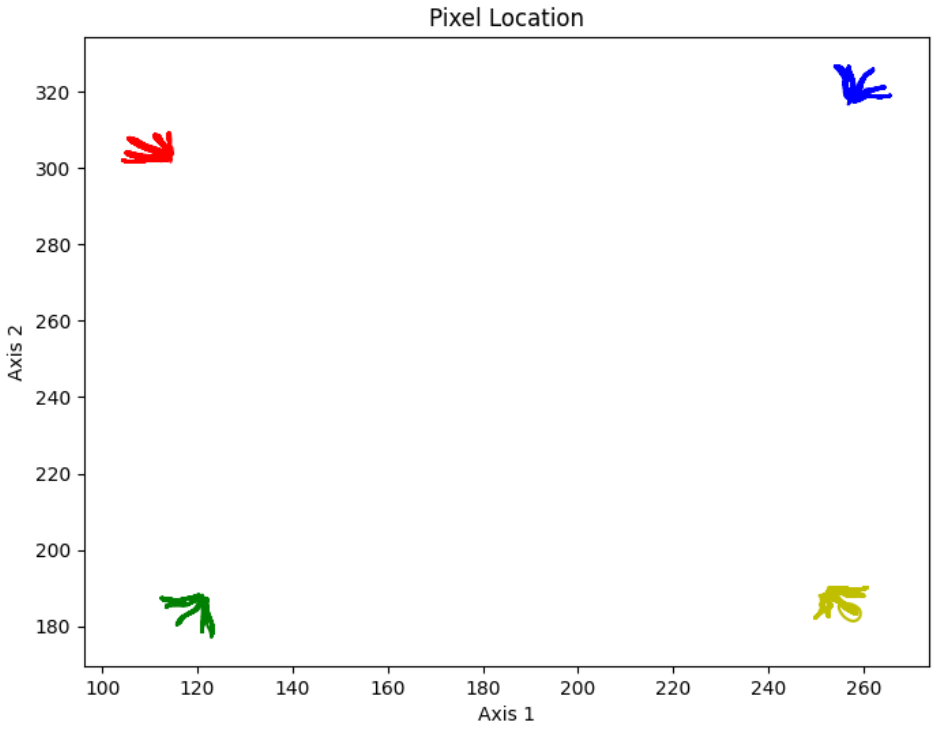

Figure 6.3. An example of Pixel Locations for Female SuHx Rat 170 Trial 3. Each color represents one of the four markers that are tracked and used to calculate strain at the center of the tissue, and the shape formed as the marker moves shows five projections that correspond to the five different stretch ratios that occur during the test.

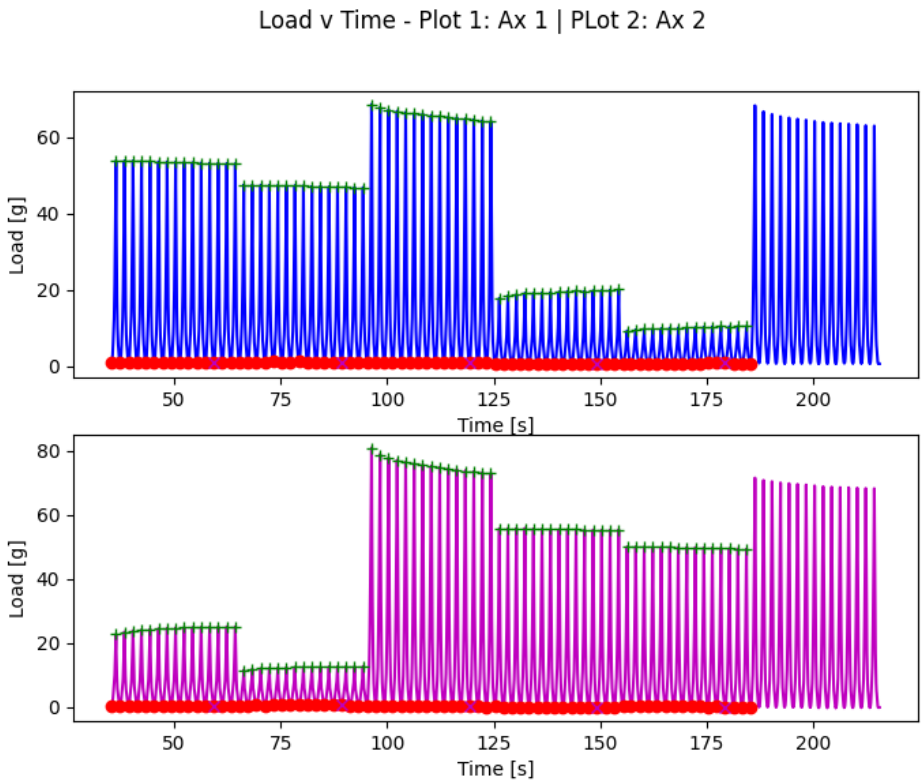

Figure 6.4. An example of Load data for Female SuHx Rat 170 Trial 3. Data is graphed for blocks 2-7 of the trial, with red and green markers placed on the troughs and peaks, respectively, for blocks 2-6. The various stretch ratios for the different blocks can be observed in the varied amplitudes of the peaks, which are roughly equal for 15 stretches at a time before relocating when the next block starts. Some mild drift of the load cells is visible in the troughs of the figure, which should ideally be a straight line level at 0 grams.

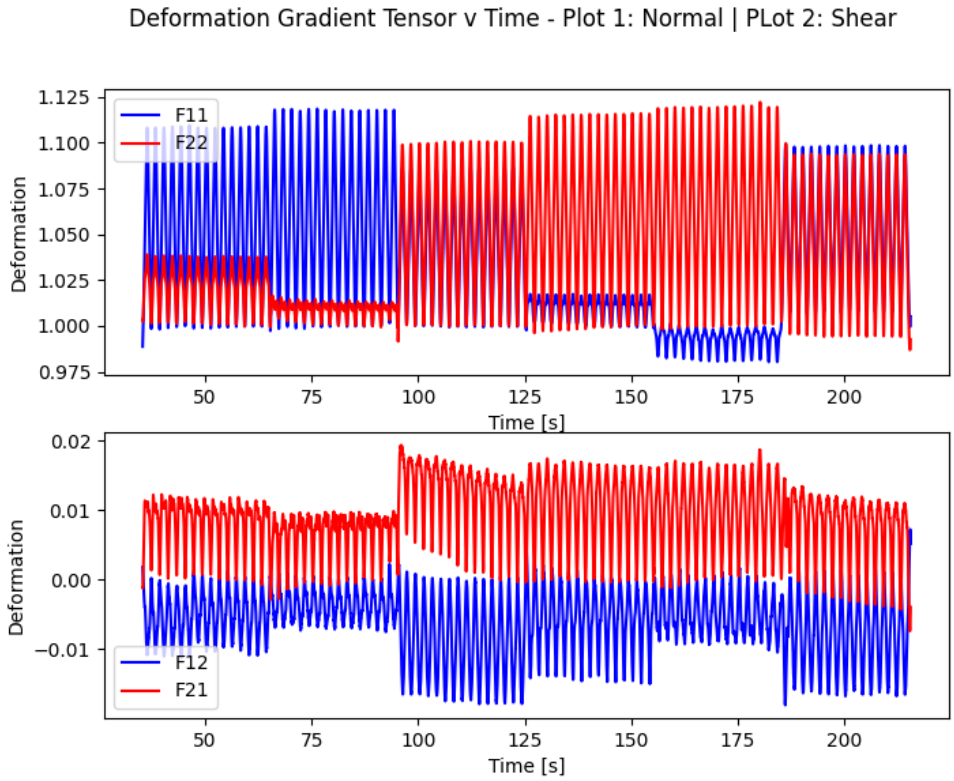

Figure 6.5. An example of Deformation gradient tensor data for Female SuHx Rat 170 Trial 3. The top figure shows the normal components while the bottom shows shear components. Note the difference in scale on the y-axis between the two. Normal components range from slightly below 1.000 to 1.125, while shear components stay within ± 0.02.

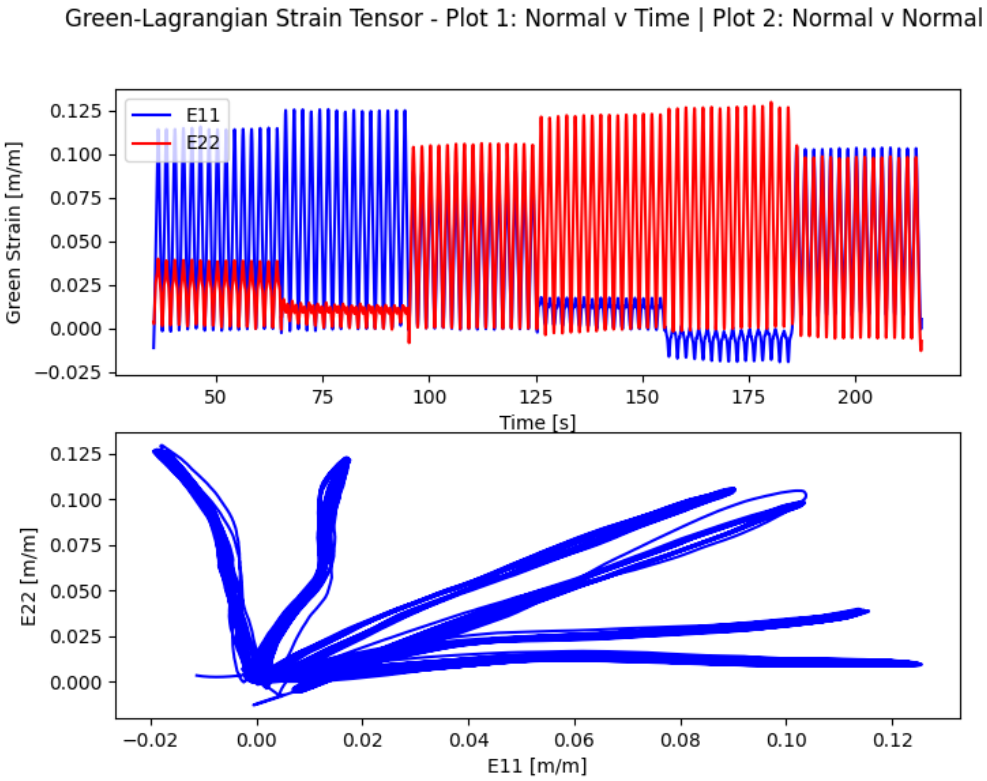

Figure 6.6. An example of Green-Lagrangian strain tensor data for Female SuHx Rat 170 Trial 3. The top figure shows the normal strains versus time, and the bottom figure shows the two plotted against each other, where you can again see five projections representing the five different stretch ratios. The middle projection represents the equibiaxial stretch ratio, and shows up as two projection groups because there are multiple test block with equibiaxial stretching.

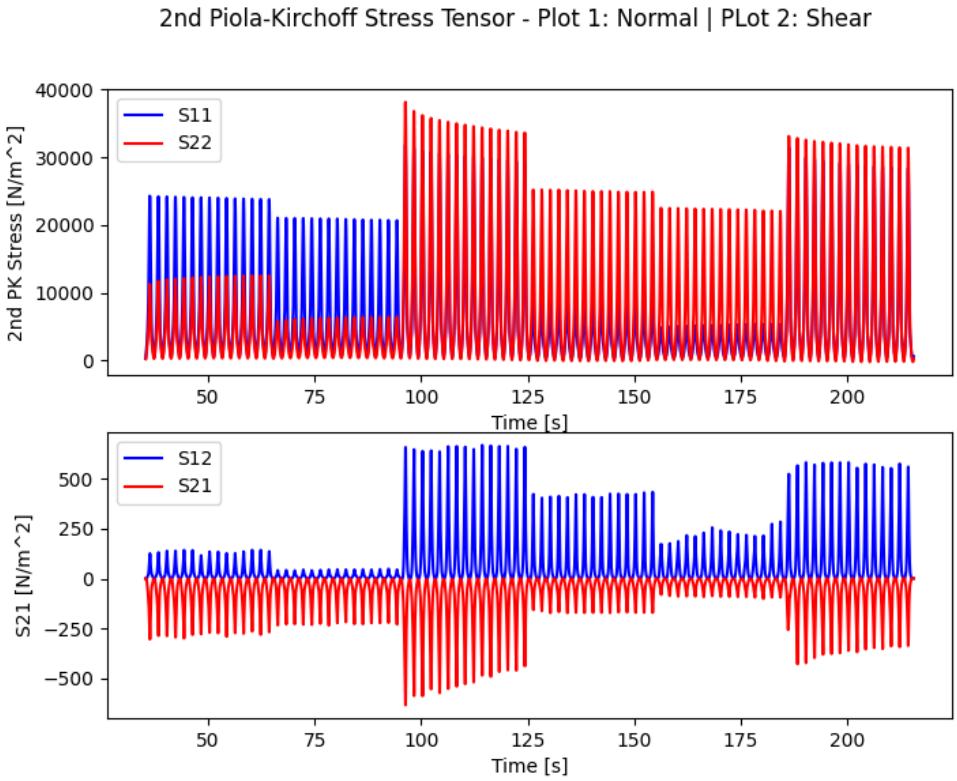

Figure 6.7. An example of 2nd Piola-Kirchhoff stress tensor data for Female SuHx Rat 170 Trial 3. The top figure shows normal components of the stress tensor, while the bottom shows shear components, which we can observe to be relatively close to zero compared to the normal components.

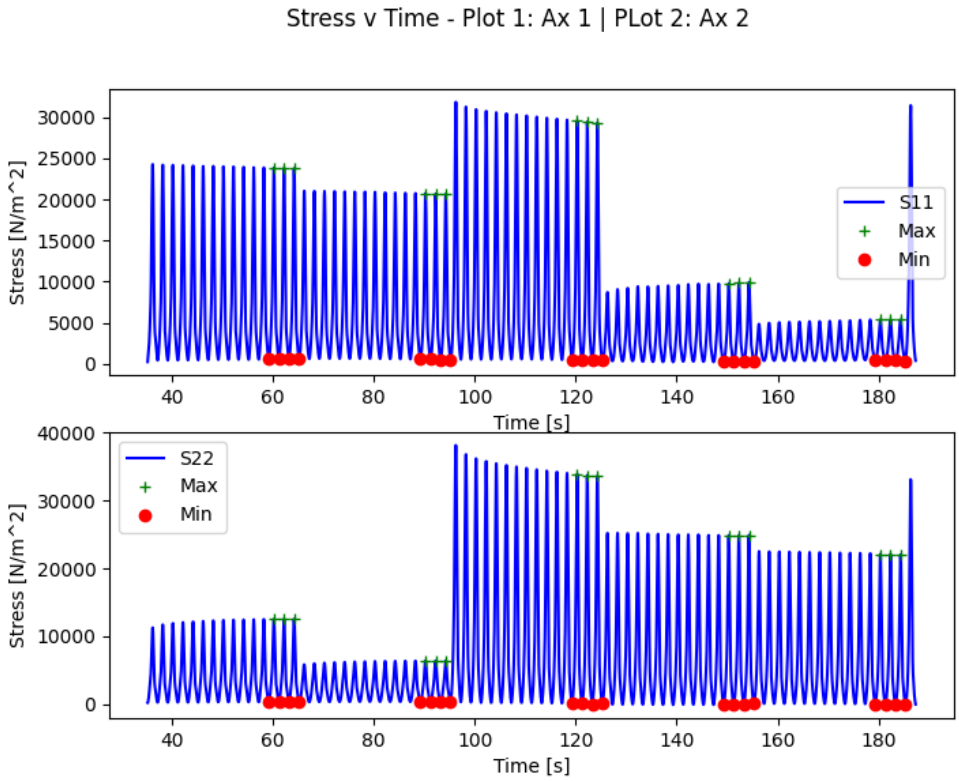

Figure 6.8. An example of stress tensor data for Female SuHx Rat 170 Trial 3, with the normal stresses in apex-outflow and circumferential directions plotted separately. Again, red and green markers identify the troughs and peaks of the stresses, and here they are placed on the last three stretch cycles of each block, which are later averaged and used for modeling.

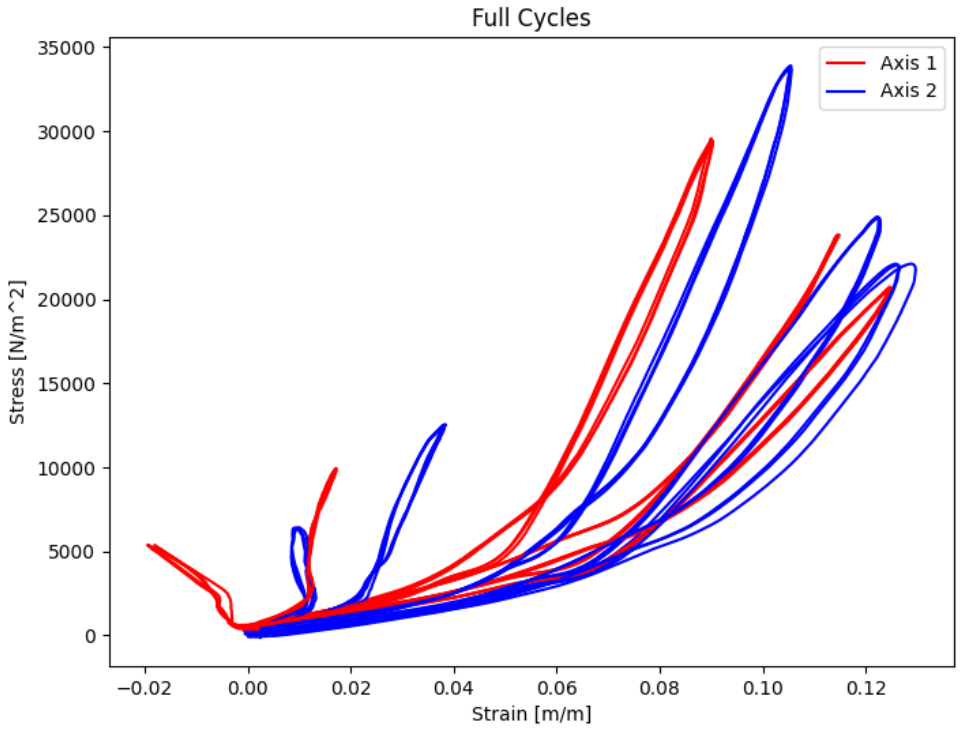

Figure 6.9. An example of the three selected stress versus strain curves for Female SuHx Rat 170 Trial 3. Each axis has five general loops corresponding to the five different stretch ratios in the trial, and each of these loops has three curves plotted to assess overlap and shape.

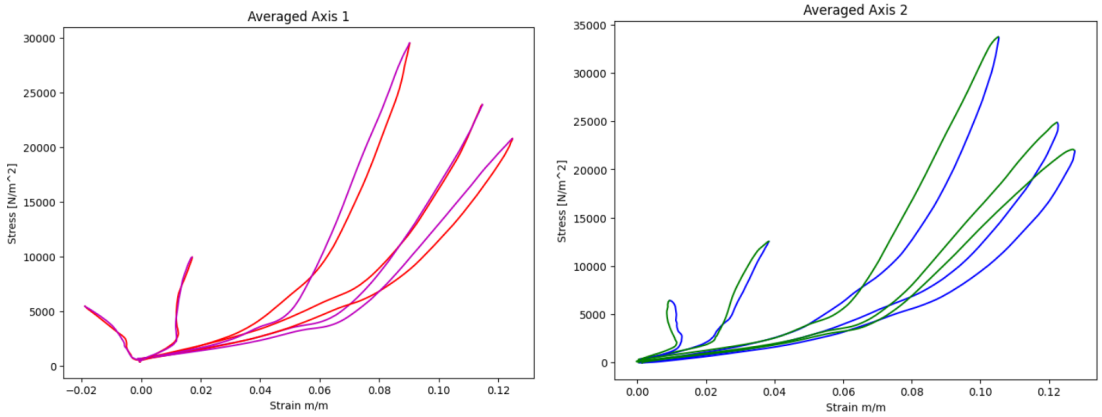

(a) (b)

Figure 6.10. The three curves plotted for each loop in Figure 6.9 are averaged to obtain plots for the averaged loops in (a) Axis 1 and (b) Axis 2.

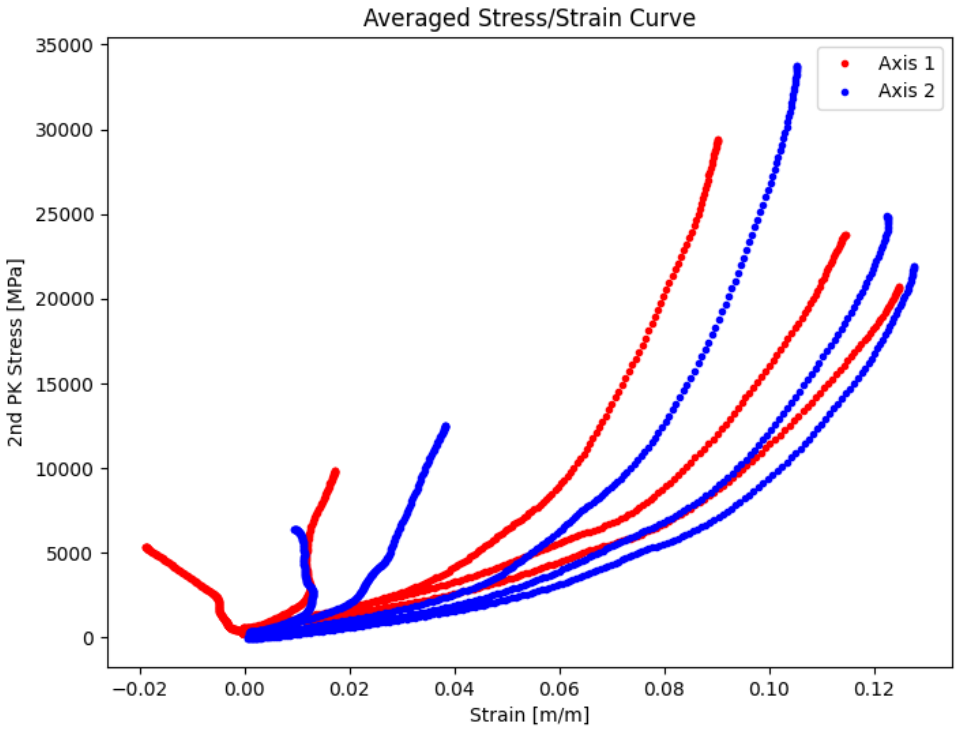

Figure 6.11. An example of the final averaged stress versus strain loading curves for Female SuHx Rat 170 Trial 3.

Chapter 7

Mechanics Analysis - Models and Calculations

7.1 Stress

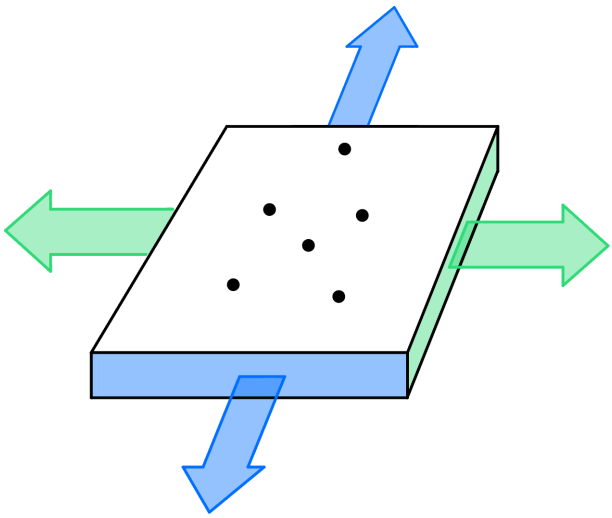

Figure 7.1. A schematic of the RV free wall sample, with arrows indicating the forces along the two axes. Blue arrows indicate axis 1 (apex-outflow direction), which is identified with a marker on the outflow edge of the tissue – five additional markers near the center are used for tracking deformation, the middle of which is used only for the camera software and not in analysis. Green arrows indicate axis 2 (circumferential). Forces act over the area shaded with the corresponding color.

Forces applied to the tissue in this experiment act over an area given by the product of length (or width, depending on the axis of interest) and thickness of the sample (Figure 7.1). Thus the half-Lagrangian stress (σ) is calculated using the dimensions of the undeformed tissue

sample and the current load, converted to Newtons. We do not have the deformed area and are therefore unable to calculate the Cauchy stress.

$$\sigma = \frac{load}{area}(0.0098) \tag{7.1}$$

Since this is the half-Lagrangian stress tensor, to properly model the stress-strain relationship we use Nanson's formula to convert everything to the undeformed area. To have the full/symmetric Lagrangian stress tensor, multiply by the inverse transpose of **F**:

$$\mathbf{P} = \sigma \mathbf{F}^T \tag{7.2}$$

P is the Lagrangian 2nd Piola-Kirchhoff stress tensor, but we use the half-Lagrangian stress because for small deformations, differences between the two vanish.

7.2 Strain

Because we are interested in studying the behavior near the center of the tissue, we compute and analyze strain from the marker positions captured by the camera (markers indicated in Figure 7.1). Strain measures the local differences between displacement and the rigid body component of this displacement, accounting for only length change and no angle change between neighboring particles.

7.2.1 Isoparametric mapping

Deformation undergone by the sample during biaxial testing is measured optically. The four markers placed on the epicardium are tracked with the camera. The pixel position sampled at 200 Hz are organized as x- and y-positions of the four square markers on the tissue, where they first need to be converted to vectors relating the current and reference marker configurations. Taking the first recorded position from each block as the reference coordinate (denoted capital X,Y), the displacement vectors u and v are calculated for the x- and y-directions, respectively,

for markers *i*=1:4.

$$u_i = x_i - X_{i,ref} \tag{7.3}$$

$$v_i = y_i - Y_{i,ref}$$

The deformation gradient **F** is defined as the displacement gradient plus the identity matrix I, represented mathematically as:

$$\mathbf{F} = \begin{bmatrix} \frac{\partial u}{\partial X} + I & \frac{\partial u}{\partial Y} \\ \\ \frac{\partial v}{\partial X} & \frac{\partial v}{\partial Y} + I \end{bmatrix} \tag{7.4}$$

In order to perform this calculation it is necessary to map nodes from the pixel positions in $x-y$ space to an idealized coordinate system in $s-r$ space. Global coordinates map to local coordinates via shape functions with the properties of the Kronecker delta and polynomial completeness. For four nodes, the shape functions are:

$$N_1(s,r) = \frac{1}{4}(1+s)(1+r)$$

$$N_2(s,r) = \frac{1}{4}(1-s)(1+r)$$

$$N_3(s,r) = \frac{1}{4}(1-s)(1-r)$$

$$N_4(s,r) = \frac{1}{4}(1+s)(1-r)$$

So that the position vectors x and y can be described by:

$$x = \Sigma_{i=1}^{4} N_i(s,r)x_i$$

$$y = \Sigma_{i=1}^{4} N_i(s,r)y_i$$

From the chain rule, we must then calculate the following partial derivatives in order to determine **F**.

$$\frac{\partial u}{\partial X} = \frac{\partial u}{\partial r}\frac{\partial r}{\partial X} + \frac{\partial u}{\partial s}\frac{\partial s}{\partial X}$$

$$\frac{\partial u}{\partial Y} = \frac{\partial u}{\partial r}\frac{\partial r}{\partial Y} + \frac{\partial u}{\partial s}\frac{\partial s}{\partial Y}$$

$$\frac{\partial v}{\partial X} = \frac{\partial v}{\partial r}\frac{\partial r}{\partial X} + \frac{\partial v}{\partial s}\frac{\partial s}{\partial X}$$

$$\frac{\partial v}{\partial Y} = \frac{\partial v}{\partial r}\frac{\partial r}{\partial Y} + \frac{\partial v}{\partial s}\frac{\partial s}{\partial Y}$$

The partial derivatives of r and s cannot be calculated directly, so we must form a Jacobian matrix **J**:

$$\mathbf{J} = \begin{bmatrix} \frac{\partial X}{\partial r} & \frac{\partial X}{\partial s} \\ \\ \frac{\partial Y}{\partial r} & \frac{\partial Y}{\partial s} \end{bmatrix} \tag{7.5}$$

So that using the determinant of **J** we can obtain:

$$\begin{bmatrix} \frac{\partial r}{\partial X} & \frac{\partial s}{\partial X} \\ \\ \frac{\partial r}{\partial Y} & \frac{\partial s}{\partial Y} \end{bmatrix} = \frac{1}{det(\mathbf{J})} \begin{bmatrix} \frac{\partial Y}{\partial s} & -\frac{\partial X}{\partial s} \\ \\ -\frac{\partial Y}{\partial r} & \frac{\partial X}{\partial r} \end{bmatrix}$$

And the partial derivatives needed to calculate **F** become:

$$\frac{\partial u}{\partial X} = \frac{\partial u}{\partial r}\frac{1}{det(\mathbf{J})}\frac{\partial Y}{\partial s} + \frac{\partial u}{\partial s}\frac{-1}{det(\mathbf{J})}\frac{\partial X}{\partial s}$$

$$\frac{\partial u}{\partial Y} = \frac{\partial u}{\partial r}\frac{-1}{det(\mathbf{J})}\frac{\partial Y}{\partial r} + \frac{\partial u}{\partial s}\frac{1}{det(\mathbf{J})}\frac{\partial X}{\partial r}$$

$$\frac{\partial v}{\partial X} = \frac{\partial v}{\partial r}\frac{1}{det(\mathbf{J})}\frac{\partial Y}{\partial s} + \frac{\partial v}{\partial s}\frac{-1}{det(\mathbf{J})}\frac{\partial X}{\partial s}$$

$$\frac{\partial v}{\partial Y} = \frac{\partial v}{\partial r}\frac{-1}{det(\mathbf{J})}\frac{\partial Y}{\partial r} + \frac{\partial v}{\partial s}\frac{1}{det(\mathbf{J})}\frac{\partial X}{\partial r}$$

7.2.2 Coordinate-free strain

So far, the deformation undergone by the tissue is subject to a coordinate system. Thus, to make the motion coordinate free, we compute strain. Using the Lagrangian approach, we compute the Green strain **E** based on the Right-Cauchy Green tensor **C**:

$$\mathbf{E} = \frac{1}{2}(\mathbf{C} - \mathbf{I}) \tag{7.6}$$

where

$$\begin{aligned}
\mathbf{C} &= \mathbf{F}^T\mathbf{F} \\
&= (\mathbf{RU})^T(\mathbf{RU}) \\
&= \mathbf{U}^T\mathbf{R}^T\mathbf{RU} \\
&= \mathbf{U}^T\mathbf{IU} \\
&= \mathbf{U}^2
\end{aligned}$$

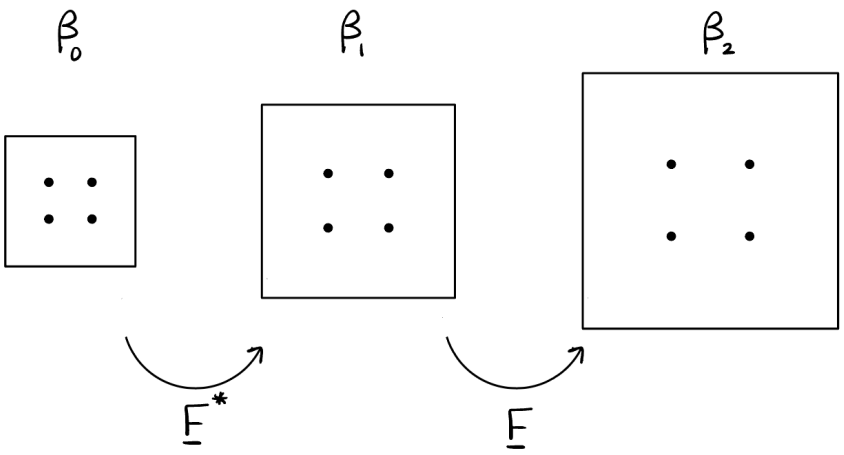

Figure 7.2. Mapping from β_0 to β_2 using $\mathbf{F}^*$ and $\mathbf{F}$.

We are now left with a measure of strain that is rotation free. If we look more closely at the Right Cauchy-Green tensor in the short derivation above, we can see that using rotation and stretch as defined in Section 7.2.4, it simplifies to the square of stretch, leaving us with a strain that is, as a result, a squared measure of length.

7.2.3 Mapping between configurations

In order to map from the unloaded state (β_0) to the current configuration (β_2), we must utilize the tare-loaded reference configuration (β_1), as diagrammed in Figure 7.2, where ($\mathbf{F}^*$) maps from β_0 to β_1 and ($\mathbf{F}$) maps from β_1 to β_2. The deformation gradient that maps from β_0 to β_2 can then be obtained from the product of the two single-step deformation gradients: ($\mathbf{F}^*\mathbf{F}$). The shear components of $\hat{\mathbf{E}}$ were negligible in all test specimens, so only the normal apex-outflow tract and circumferential components $\hat{\mathbf{E}}_{\mathbf{11}}$ and $\hat{\mathbf{E}}_{\mathbf{22}}$ were analyzed. Using this total deformation, the Green strain tensor $\hat{\mathbf{E}}$ can be reformulated in terms of the experimental stretches Λ_i (β_1 to β_2):

$$\hat{\mathbf{F}} = \mathbf{F}^*\mathbf{F}$$

$$\hat{\mathbf{E}} = \frac{1}{2}(\hat{\mathbf{F}}^{\mathbf{T}}\hat{\mathbf{F}} - \mathbf{I})$$

$$\hat{\mathbf{E}} = \frac{1}{2}\begin{bmatrix} (f_1F_{11})^2 + (f_2F_{21})^2 - 1 & f_1^2F_{11}F_{12} + f_2^2F_{21}F_{22} \\ \\ f_1^2F_{11}F_{12} + f_2^2F_{21}F_{22} & (f_1F_{12})^2 + (f_2F_{22})^2 - 1 \end{bmatrix}$$

$$\hat{\mathbf{E}} = \frac{1}{2}\begin{bmatrix} f_1^2\Lambda_1^2 - 1 & 0 \\ \\ 0 & f_2^2\Lambda_2^2 - 1 \end{bmatrix} \tag{7.7}$$

Here, the diagonal components of $\mathbf{F}^*$ (f_1 and f_2) are the pre-stretches, estimated in terms of the experimental stretches:

$$f_1 = \sqrt{\frac{E_{11}\Lambda_2}{\Lambda_1} + 1}\ ,\ f_2 = \sqrt{\frac{E_{22}\Lambda_1}{\Lambda_2} + 1}$$

7.2.4 Polar Decomposition

Another use of the deformation computed from isoparametric mapping is in determining how much of the deformation undergone by the tissue is attributed to stretch versus rotation. This can be done by performing polar decomposition, where the deformation gradient tensor $\mathbf{F}$ is the product of rotation $\mathbf{R}$ and stretch $\mathbf{U}$, in that order: $\mathbf{F} = \mathbf{RU}$. The rotation tensor is a proper orthogonal tensor that measures local rotation, and the right stretch tensor is a positive definite and symmetric tensor. Mathematically, we perform the decomposition by first obtaining the symmetric right Cauchy-Green deformation tensor $\mathbf{C}$, where:

$$\mathbf{C} = \mathbf{F}^T\mathbf{F} = \mathbf{U}^2$$

$\mathbf{C}$ must then be diagonalized by finding its positive real eigenvalues and corresponding

tensor **N** of normalized eigenvectors, and stretch **U** can then be calculated.

$$\mathbf{U} = \mathbf{N}\sqrt{\mathbf{C}}\mathbf{N}^T$$

To complete the decomposition, **R** is calculated using **F** and the inverse of **U**.

$$\mathbf{R} = \mathbf{F}\mathbf{U}^{-1}$$

By observing R and U independently, we can separate rigid body translations and rotations from deformations, which are the sources of stresses and provide more mechanical interest.

7.3 Constitutive Model - Parameter Estimation

By assuming the RV myocardium to be an incompressible planar hyperelastic material, we proposed it be described by the following two-dimensional Fung-type exponential strain-energy function:

$$W(\hat{\mathbf{E}}) = C(e^{Q(\hat{\mathbf{E}})} - 1) \tag{7.8}$$

where

$$Q(\hat{\mathbf{E}}) = \hat{a}_1\hat{E}_{11}^2 + \hat{a}_2\hat{E}_{22}^2 + \hat{a}_3\hat{E}_{11}\hat{E}_{22}$$

is the Green strain tensor $\hat{\mathbf{E}}$ referenced to the unloaded state β_0. Following from this, the PK2 stress with respect to β_0 is

$$\hat{\mathbf{S}} = \frac{\partial W(\hat{\mathbf{E}})}{\partial \hat{\mathbf{E}}} = C\frac{\partial e^{Q(\hat{\mathbf{E}})}}{\partial \hat{\mathbf{E}}}\frac{\partial \hat{\mathbf{E}}}{\partial \Lambda}$$

We can then expand the partial derivatives component-wise in terms of the experimental stretches,

$$\hat{S}_{11} = C\frac{\partial e^{Q(\hat{\mathbf{E}})}}{\partial \hat{E}_{11}}\frac{\partial \hat{E}_{11}}{\partial \Lambda_1} = Ce^{Q(\hat{\mathbf{E}})}\frac{\partial Q(\hat{\mathbf{E}})}{\partial \hat{E}_{11}}\frac{\partial \hat{E}_{11}}{\partial \Lambda_1} = Ce^{Q(\hat{\mathbf{E}})}(2\hat{a}_1\hat{E}_{11} + \hat{a}_3\hat{E}_{22})f_1^2\Lambda_1$$

$$\hat{S}_{11} = C\frac{\partial e^{Q(\hat{\mathbf{E}})}}{\partial \hat{E}_{11}}\frac{\partial \hat{E}_{11}}{\partial \Lambda_1} = Ce^{Q(\hat{\mathbf{E}})}\frac{\partial Q(\hat{\mathbf{E}})}{\partial \hat{E}_{11}}\frac{\partial \hat{E}_{11}}{\partial \Lambda_1} = Ce^{Q(\hat{\mathbf{E}})}(2\hat{a}_1\hat{E}_{11} + \hat{a}_3\hat{E}_{22})f_1^2\Lambda_1$$

$$\hat{S}_{12} = \hat{S}_{21} = 0$$

This results in the diagonal tensor

$$\hat{\mathbf{S}} = C\begin{bmatrix} e^{Q(\hat{\mathbf{E}})}(2\hat{a}_1\hat{E}_{11} + \hat{a}_3\hat{E}_{22})f_1^2\Lambda_1 & 0 \\ 0 & e^{Q(\hat{\mathbf{E}})}(2\hat{a}_2\hat{E}_{22} + \hat{a}_3\hat{E}_{11})f_2^2\Lambda_2 \end{bmatrix}$$

Next we can plug in the normal strain components derived above to obtain a stress tensor completely in terms of unloaded to reference configuration deformations and experimental stretches, where again the only non-zero components are $\hat{\mathbf{S}}_{\mathbf{11}}$ and $\hat{\mathbf{S}}_{\mathbf{22}}$:

$$\hat{S}_{11} = Cf_1^2e^{Q(\Lambda)}(\hat{a}_1(f_1^2\Lambda_1^2 - 1) + \frac{\hat{a}_3}{2}(f_2^2\Lambda_2^2 - 1))\Lambda_1$$

$$\hat{S}_{22} = Cf_2^2e^{Q(\Lambda)}(\hat{a}_2(f_2^2\Lambda_2^2 - 1) + \frac{\hat{a}_3}{2}(f_1^2\Lambda_1^2 - 1))\Lambda_2$$

where

$$Q(\Lambda) = \frac{1}{4}(\hat{a}_1(f_1^2\Lambda_1^2 - 1)^2 + \hat{a}_2(f_2^2\Lambda_2^2 - 1)^2 + \hat{a}_3(f_1^2\Lambda_1^2 - 1)(f_2^2\Lambda_2^2 - 1))$$

Computing model parameters for each individual animal (Figure 7.3) allows us to generate

strain-energy values for all strain combinations, resulting in a surface which can be averaged with others for comparisons between groups (Figure 7.4).

7.3.1 Numerical Implementation

Parameters for the above model are determined by minimizing the following objective function, which computes a difference between the experimentally-derived stress tensor $S_{ii}(t_j)$ and the model stress tensor $S_{ii}^M(t_j;\theta)$. This function:

$$\phi(\theta) = \Sigma_i^2 \Sigma_j^n (S_{ii}(t_j) - S_{ii}^M(t_j;\theta))^2 \tag{7.9}$$

solves for θ which is the set of parameters $\{C, a_1, a_2, a_3, f_1, f_2\}$. The function is minimized in Python using the L-BFGS optimization algorithm, a limited-memory quasi-Newton approximation of the Broyden–Fletcher–Goldfarb–Shanno algorithm. Optimized parameters are output from the Python code and stored in a model parameter database.

Following optimization, the parameters are used to generate a strain-energy surface for each individual animal, which can then be point-wise averaged within groups. Surface generation is performed in Python, and the 10% equibiaxial stress-strain projections are exported to Prism where they are averaged for comparison between groups.

7.4 Statistical Analysis

For group comparisons of hemodynamic metrics, morphological measurements, and mechanical data descriptive statistics were conducted using JMP Pro Statistical software (version 17, SAS Institute Inc., NC, USA). Two-factor ANOVA was employed for normally-distributed data to test for differences based on treatment stage (control, Early-, Mid-, and Late-stage SuHx) and animal group (male, intact female, and ovariectomized female) followed by the Tukey test for comparisons within these variables. Three-factor ANCOVA was used for continuous stress data, which underwent a linear transformation to log(stress+1), to test for differences based on strain,

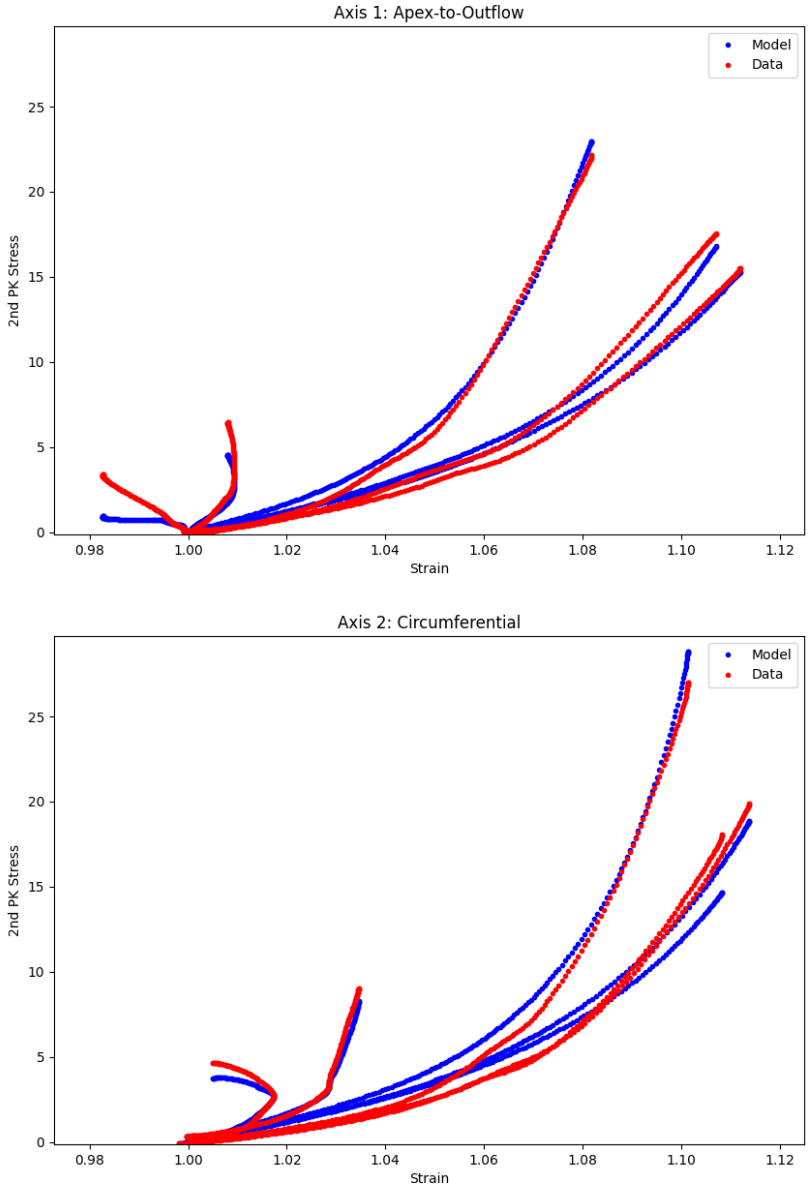

Figure 7.3. Example of model fit for experimental stress-strain data. Data is shown in red, model in blue. Data is from female SuHx Rat number 170, Trial 2.

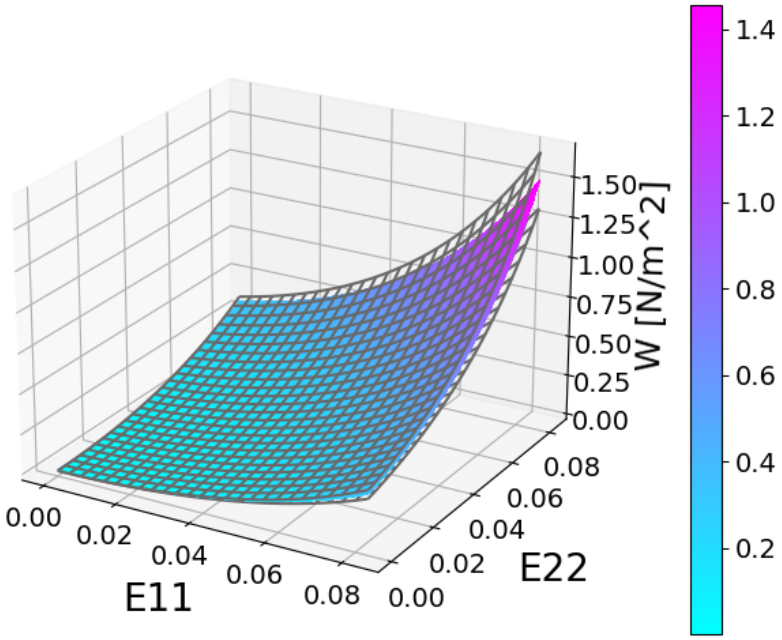

Figure 7.4. Example of averaged strain-energy surface. Model is computed from 0-8% strain in each direction, with average displayed as a color gradient from cyan to magenta, $\pm$ standard error in grey. Example is from Female SuHx rats in Early weeks (3, 4 and 6).

treatment stage, and group. Where applicable, the Tukey test was again used for comparison within these variables.

Chapter 8

Results

Male, intact female, and ovariectomized female rats were treated with SuHx to induce PAH, and after a specified time of disease progression (Table 8.1), *in vivo* pressure-volume hemodynamic measurements were recorded (Section 3.2), and the right-ventricle was excised and subjected to planar biaxial mechanical testing, both before and after decellularization (Section 5). This section presents the results of these experiments.

Table 8.1. Time points (weeks) included in disease stages for analysis of PAH progression.

Disease Stage	Weeks Included
Early	3, 4, 6
Mid	8
Late	10, 12, 15

Table 8.2. Sample sizes for intact male, female, and OVX control and PAH groups.

Group:	Male	Female	OVX
Control	14	18	19
Early	12	12	7
Mid	11	9	8
Late	9	13	13

8.1 PAH Confirmation & Tissue Morphology

Of the 145 animals used in this study, 94 were injected with Sugen and placed in hypoxia to develop PAH. The non-treated animals were kept in normoxia for the entire time period. PAH

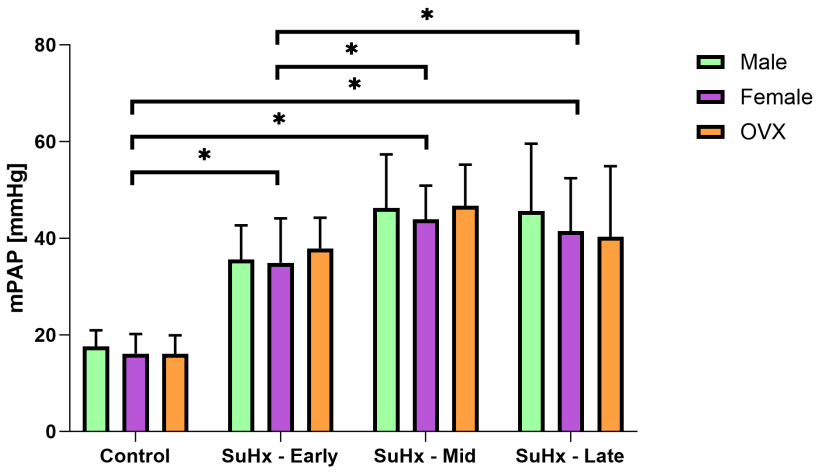

Figure 8.1. Mean pulmonary arterial pressures for control and SuHx rats. Males (green), intact females (purple) and OVX females (orange) all increase significantly from control to SuHx, and from Early-stage to Mid- and Late-stage. No differences between groups are significant. Data shown as mean $\pm$ standard error (SE). * $p < 0.05$ comparison between SuHx stages.

was confirmed with mPAP greater than 20 mmHg (Figure 8.1). MPAP were significantly higher in the SuHx animals compared with their respective control groups ($p < 0.0001$). For all groups, mPAP increased significantly ($p = 0.0002$) from Early- to Mid-stage PAH. The increase from Early- to Late-stage was also significant ($p = 0.0189$). Late-stage mPAPs are slightly lower than Mid-stage, but this difference is not significant ($p = 0.5142$). Group was not found to be significant.

RV thickness was found to increase from control to all stages of SuHx development, but the increases differ between groups (Figure 8.2). Males continue to increase through to Late-stage PAH, whereas intact females peak at week 8, and OVX females peak at Early-stage. Due to a significant interaction between group and SuHx stage, none of these differences are statistically significant.

RV mass was found to have significant changes due to both group and treatment stage (Figure 8.3). Intact females were found to be significantly different from both males ($p < 0.0001$) and OVX females ($p = 0.0029$). The difference between males and OVX females was

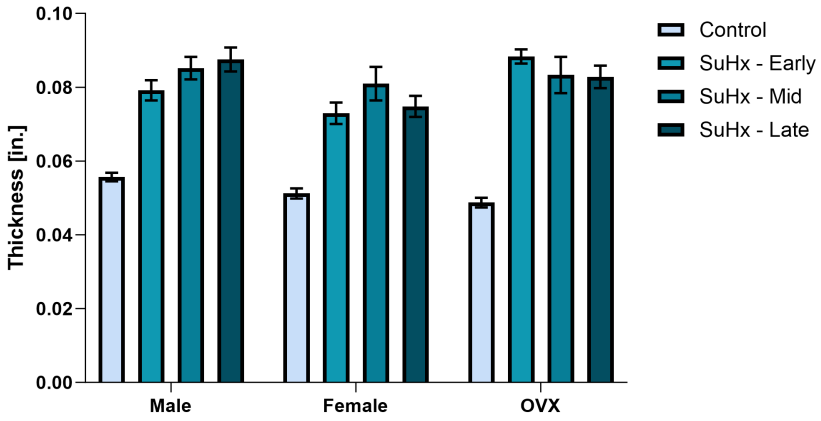

Figure 8.2. RV thickness for male, intact female, and OVX female rats at control (light blue), Early (medium teal), Mid (medium-dark teal) and Late (dark teal) SuHx. Data shown as mean $\pm$ SE. Thickness is seen to increase from control to all SuHx stages, for all groups. No differences are significant due to significant interactions.

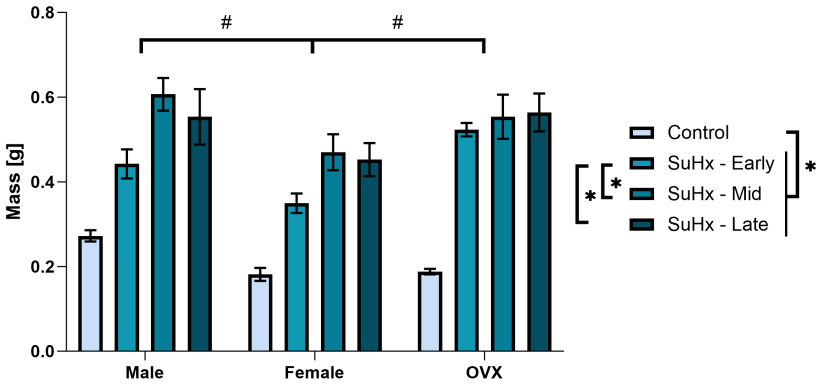

Figure 8.3. RV mass for male, intact female, and OVX female rats at control (light blue), Early (medium teal), Mid (medium-dark teal) and Late (dark teal) SuHx. Mass is significantly different between male and intact female, and between OVX and intact female groups, and increases in all SuHx stages compared to respective controls, as well as from Early- to Mid-stage. Data shown as mean $\pm$ SE. * $p < 0.05$ comparison between SuHx stages, # $p < 0.05$ comparison between groups.

not significant ($p = 0.5122$). All stages of PAH development were found to have significantly higher mass than controls ($p < 0.0001$). Early-stage was significantly different from both Mid- ($p = 0.0008$) and Late- ($p = 0.0046$) stage. The difference between Mid-stage and Late-stage was

not significant (p = 0.8947).

8.2 Planar Biaxial Testing of Intact RV Myocardium

Mechanical testing of the intact RV myocardium, and pursuant modeling, results in a stress-strain relation for each individual animal which can be averaged with other equibiaxial curves from that group (group, disease stage as defined in Table 8.1) for a representative curve. Three-way ANCOVA of strain, group, and stage shows significant interactions ($p < 0.05$) for all variables, so we will analyze group and stage individually.

8.2.1 RV Tissue Behavior is Anisotropic in Health but not in Disease

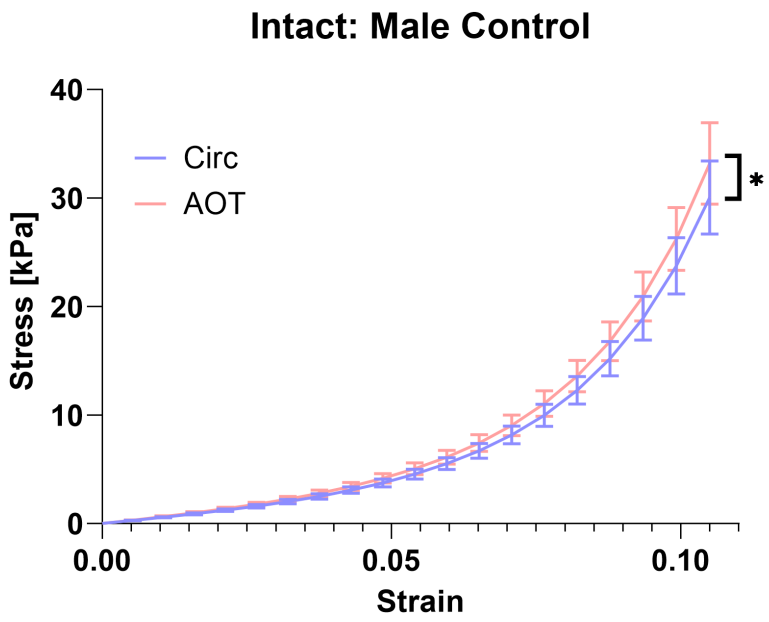

Figure 8.4. Control male equibiaxial stress-strain curves for the apex-outflow (AOT, red) and circumferential (Circ, blue) directions. Data shown as mean ± SE. * $p < 0.05$ comparison between axes.

Control males have a significant (p = 0.0024) difference between the apex-outflow (AOT) and circumferential (Circ) axes, where AOT is slightly stiffer than Circ (Figure 8.4). Differences between axes are not significant in any other groups.

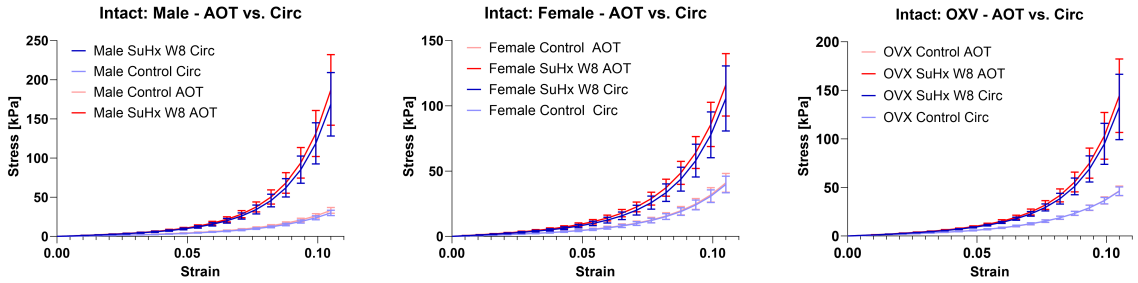

(a) (b) (c)

Figure 8.5. Comparison of stiffness in the two axes: apex-outflow (AOT, red) and circumferential (Circ, blue). Comparison is shown for Control (light) and SuHx Week 8 (dark) in (a) male, (b) female, and (c) OVX animals. Stresses increase from Control to W8 in all groups, but the two axes are not significantly different in SuHx. Note the differences in the y-axis scale between the three sub-figures. Data shown as mean $\pm$ SE.

While the AOT direction stresses are marginally higher than Circ stresses in all SuHx groups, the differences are not statistically significant (Figure 8.5). These results are consistent across all disease stages (only week 8 shown). For simplicity, the following results will focus on the AOT direction stresses, and we will assume that due to the isotropy of the SuHx tissues any findings will apply to the circumferential direction as well.

8.2.2 RV Stiffness Peaks at Week 8 of SuHx in Male and Female Rats

SuHx rats were evaluated at various weeks, and grouped into three disease stages: Early, Mid, and Late, as defined in Table 8.1. The following results will display averaged equibiaxial stress-strain curves at these stages for the evaluation of changes occurring over the course of disease progression.

Male SuHx rats display increased stresses at all stages of PAH development when compared to controls (Figure 8.6). This increase is the most pronounced at Mid-stage (Week 8), with Early- and Late-stages both occurring at lower stress levels. Due to significant interaction between stage and strain ($p < 0.0001$), differences between stages of disease development cannot be determined statistically significant.

Similar to the male group, intact female SuHx rats display increased stresses at all stages

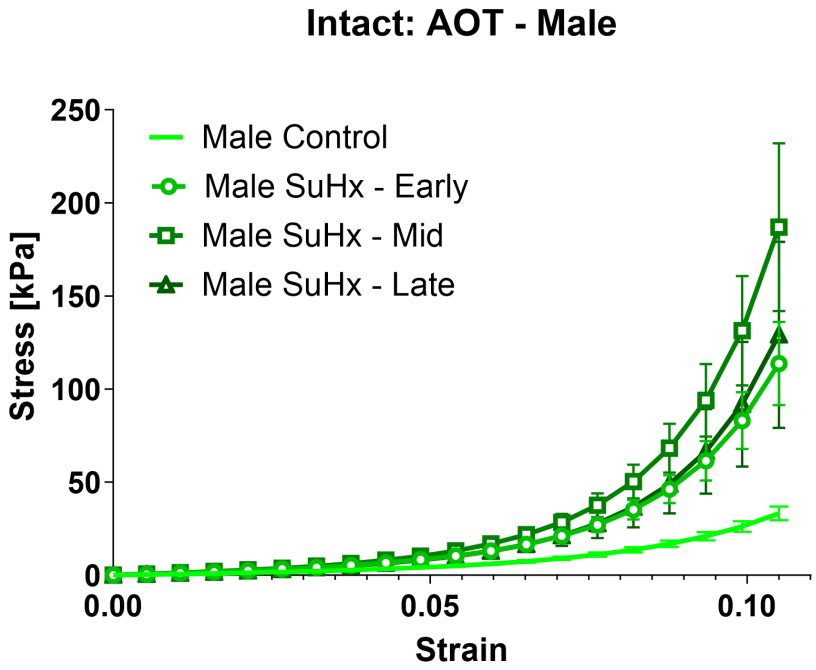

Figure 8.6. Average equibiaxial stress-strain curves for male rats at control (solid), Early-stage (circle-marked), Mid-stage (square-marked), and Late-stage (triangle-marked) of SuHx progression. Stresses are increased in all stages of disease development. Highest stresses occur at Mid-stage PAH (8 weeks post-induction). Data shown as mean $\pm$ SE. Due to significant interaction, these differences are not statistically significant.

of PAH development (Figure 8.7). This increase is again the most pronounced at Mid-stage (Week 8), with Early- and Late-stages both occurring at more modest stress levels. Due to significant interaction between stage and strain ($p < 0.0001$), differences between stages of disease development cannot be determined statistically significant.

OVX female rats (Figure 8.8) have a stress increase at all stages of PAH compared to control, but the stress-strain curves for all SuHx stages appear to overlap almost entirely, with Late-stage appearing marginally higher at 10.5% strain. Again, interactions between stage and strain are statistically significant ($p < 0.0001$), so statistical differences between stages of disease development cannot be determined.

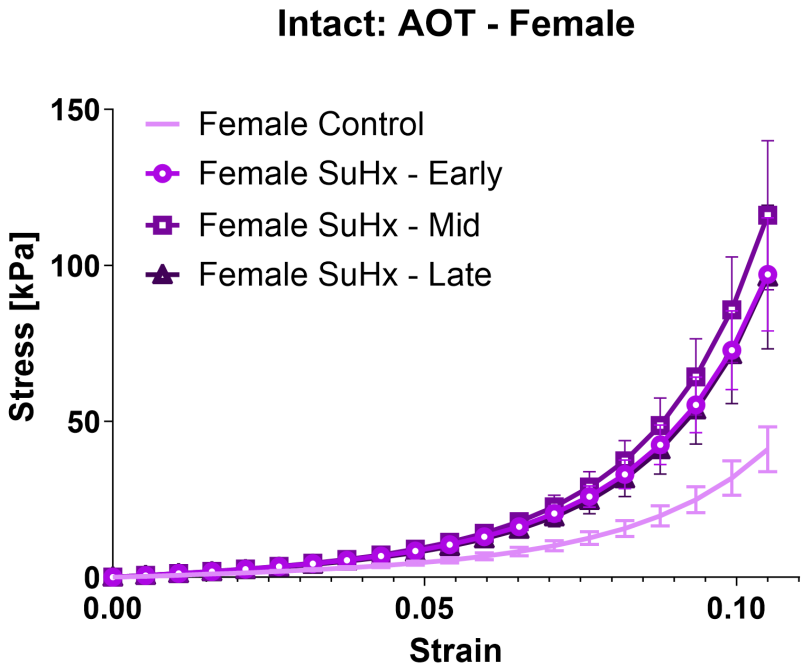

Figure 8.7. Average equibiaxial stress-strain curves for intact female rats at control (solid), Early-stage (circle-marked), Mid-stage (square-marked), and Late-stage (triangle-marked) of SuHx progression. Stresses are increased in all stages of disease development, with highest stresses occurring at Mid-stage PAH (8 weeks post-induction). Data shown as mean $\pm$ SE. Due to significant interaction, these differences are not statistically significant.

8.2.3 RV Stiffness is Sex-Dependent

Three groups stratified by sex and ovarian hormone-level were evaluated over the course of PAH progression: males, intact females (with ovarian hormones), and OVX females (with reduced ovarian hormones). The following results will compare stress-strain relations between these groups at each of the disease stages defined in Table 8.1.

We can first note that, upon comparison of the control stress-strain curves, we find that they are all quite similar, with OVX females the least compliant and males the most. No *post hoc* tests can be done to evaluate these differences due to significant interaction between sex and strain ($p = 0.0324$). This significant interaction does, however, imply that group does impact the stiffness, or stress-strain slope, of these RVs.

In the Early stage of PAH development (weeks 3, 4, and 6), we see that OVX SuHx

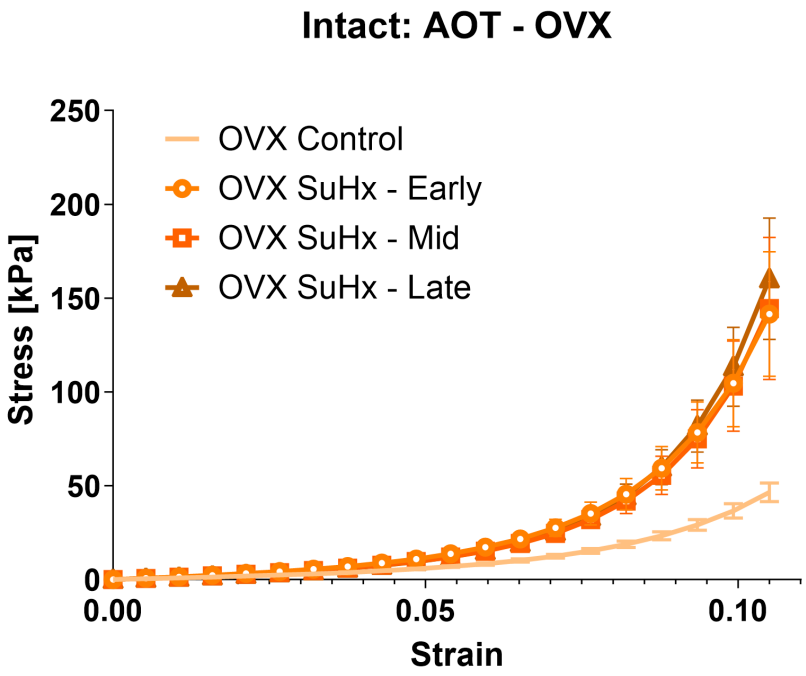

Figure 8.8. Average stress-strain curves for OVX rats at control (solid), Early-stage (circle-marked), Mid-stage (square-marked), and Late-stage (triangle-marked) of SuHx progression. All SuHx stages reach higher stresses than controls, but curves are mostly overlapping, with Late-stage only marginally higher. Data shown as mean $\pm$ SE. Due to significant interaction, no differences are statistically significant.

animals are the stiffest, while intact females are the most compliant of the diseased groups (Figure 8.9). The shapes of all three SuHx curves are similar, but we can observe that, while all appear to overlap at very small strains, the OVX curve separates at around 0.05 strain, while the male and intact female curves separate later at a strain of around 0.08. There are significant interactions between group and strain ($p = 0.0048$), as well as between treatment and strain ($p < 0.0001$) so no differences can be determined significant.

At 8 weeks of PAH development, the male RVs are the stiffest, while the intact females remain the least stiff (Figure 8.10). No differences are statistically significant due to significant interactions between group, treatment, and strain ($p < 0.0001$), so we're unable to separate the effects of treatment and group.

In Late-stage PAH (weeks 10, 12, and 15), we again see that OVX females have the

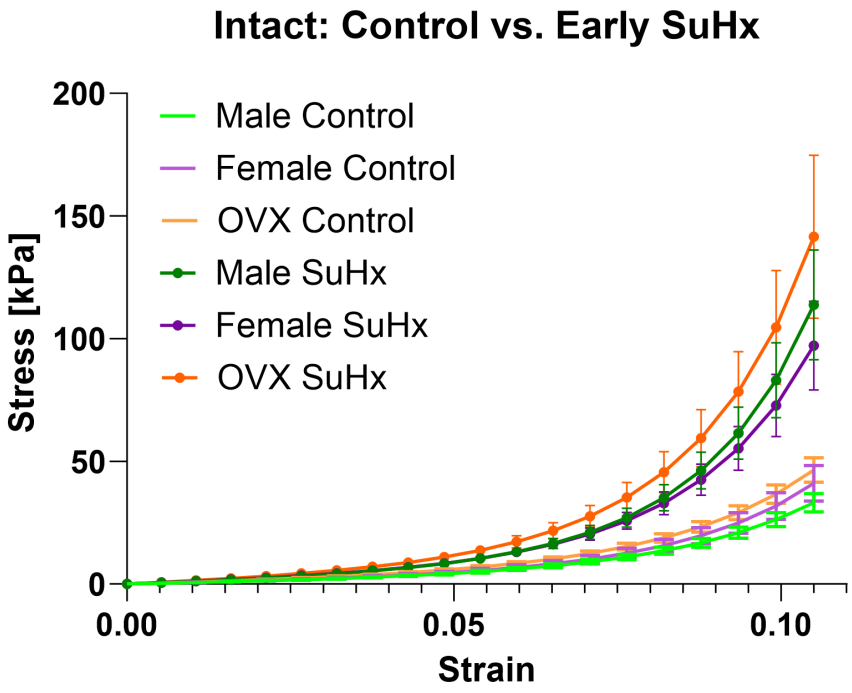

Figure 8.9. Average stress-strain curves for male (green), intact female (purple), and OVX female (orange) rats in the Early stage of SuHx progression, with controls (un-dotted lines). All three SuHx groups reach higher stresses than their respective controls, with OVX females the stiffest and intact females the most compliant. Data shown as mean $\pm$ SE. Due to significant interaction, no differences are statistically significant.

highest stresses (Figure 8.11). Intact females once again have the lowest stresses, with males falling in between the two female groups. There are again significant interactions between sex and strain as well as between treatment and strain ($p < 0.0001$) so no differences can be determined significant.

8.3 Planar Biaxial Testing of Decellularized RV

Similar to the intact myocardium, the mechanical testing and modeling of the decellularized (decell) RV results in a stress-strain relation for each individual animal which can be averaged with others from that group (sex, disease) for a representative equibiaxial curve. Only male and intact female ECM were tested, and only at control and 8 Weeks PAH. The decellularized groups are more heterogeneous than are the intact groups. Some individual animals display

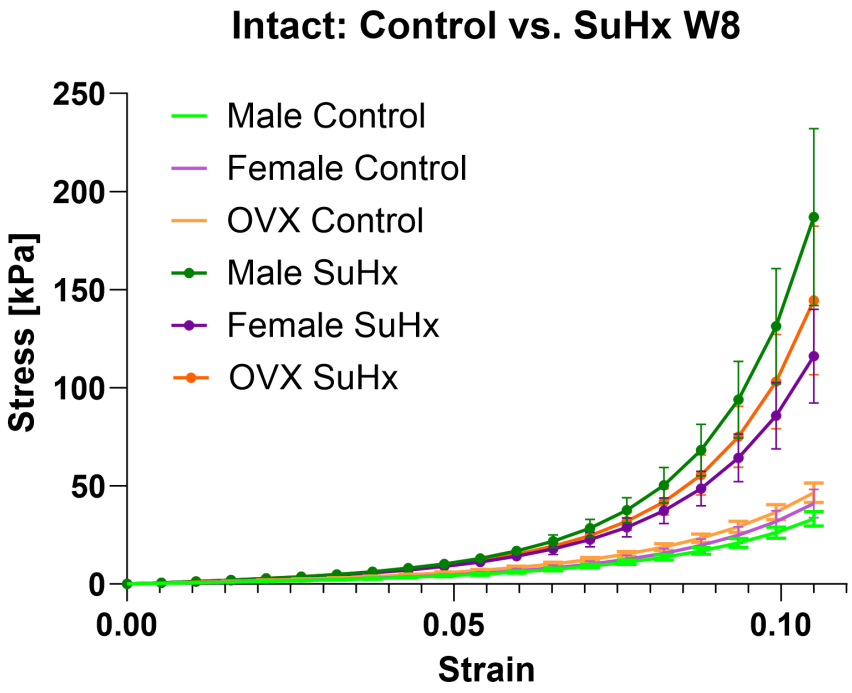

Figure 8.10. Average stress-strain curves for male (green), intact female (purple), and OVX female (orange) rats at 8 weeks of SuHx progression (Mid-stage), with controls (un-dotted lines). SuHx groups reach higher stresses than controls, with males the stiffest and females the most compliant. Data shown as mean ± SE. Due to significant interaction, no differences are statistically significant.

extremely elevated stresses when compared to the rest of the group, for example those marked with a red box in Figure 8.12. These animals, as well as similar outliers from SuHx and Female groups, have been excluded from the remainder of the results in this section. Sample sizes for each of these (refined) groups are tabulated in Table 8.3.

Table 8.3. Sample sizes for decellularized male and female control and PAH groups.

Group:	Male	Female
Control	7	11
SuHx (W8)	7	4

The thickness of decellularized tissue samples is seen to increase significantly ($p = 0.0121$) from control to PAH in both male and female groups (Figure 8.13). Controls are roughly equal for the two sexes, and males increase slightly more in PAH than do females, but the

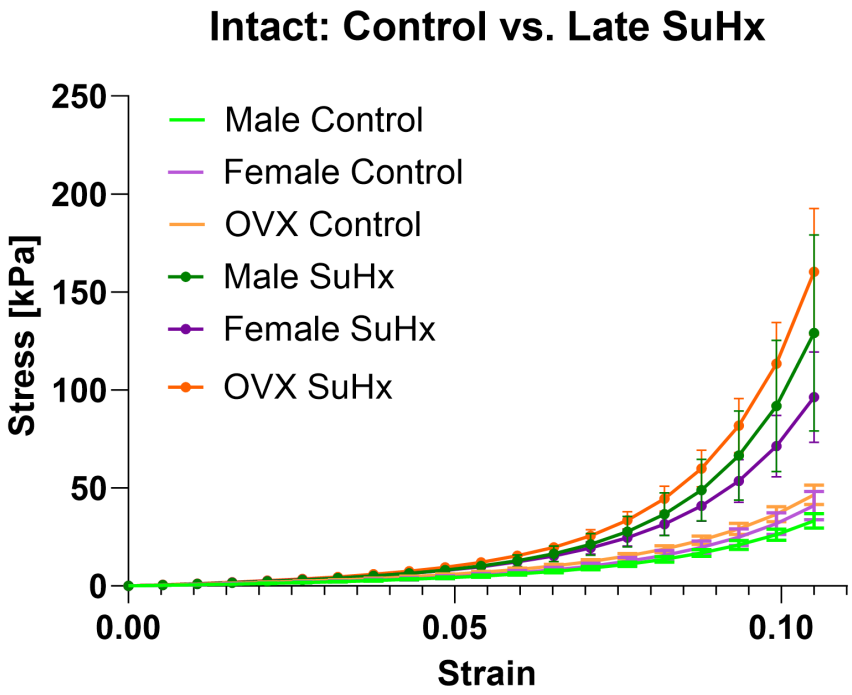

Figure 8.11. Average stress-strain curves for male (green), intact female (purple), and OVX female (orange) rats in the Late stage of SuHx progression, with controls. All SuHx groups have higher stresses than their respective controls, with OVX females the stiffest and intact females the most compliant. Data shown as mean ± SE. Due to significant interaction, no differences are statistically significant.

difference between sexes is not significant ($p = 0.9376$).

Decellularized RV mass increases significantly from control to PAH ($p = 0.0072$), and males have significantly higher mass than females ($p = 0.0420$), with no significant interactions (Figure 8.14).

8.3.1 RV ECM is Anisotropic in Female SuHx

Male control ECM is found to have a significant difference between AOT and Circ axes ($p = 0.0165$), where it can be observed that Circ has a slightly stiffer mean than does AOT (Figure 8.15). In male SuHx ECM, the AOT axis reaches higher stresses than Circ, but these differences are not statistically significant ($p = 0.3208$). This would imply that the AOT axis stiffens more in the disease, as it goes from lower stresses than Circ at control to higher in SuHx. ECM from

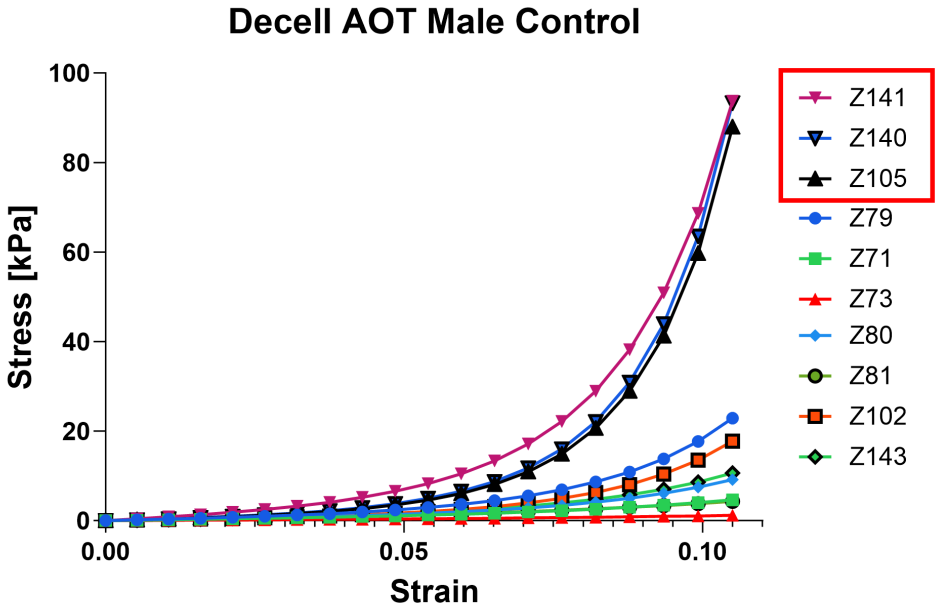

Figure 8.12. Stress-strain curves for all individual animals in the decellularized male control group. There are 10 animals in the complete group, with three clear outliers boxed in red.

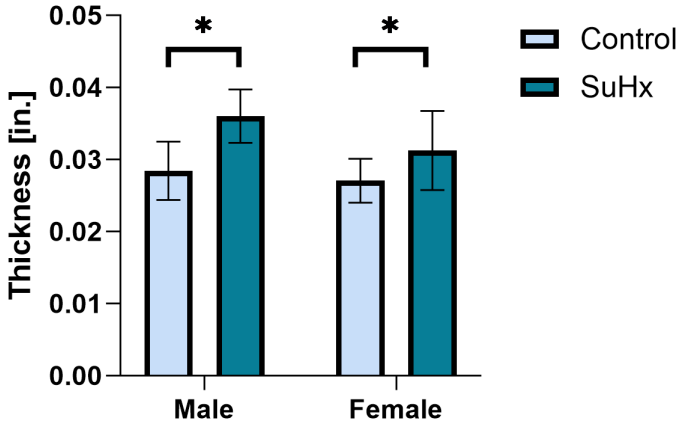

Figure 8.13. Decellularized RV thickness for control (light) and Week 8 SuHx (dark) rats. Thickness increases significantly from control to SuHx, but not between sexes. Data shown as mean $\pm$ SE. * $p < 0.05$ comparison between control and SuHx.

female control animals is not found to have statistically significant difference between AOT and Circ axes (0.0536), however this difference is found to be significant in female SuHx ECM

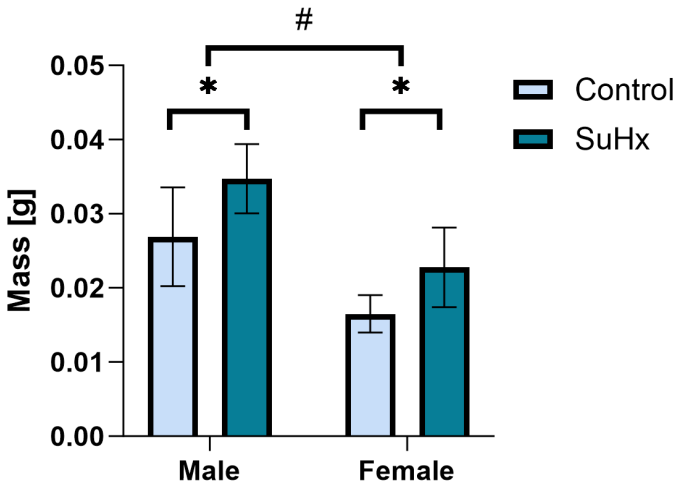

Figure 8.14. Decellularized RV mass for control (light) and Week 8 SuHx (dark) rats. Mass increases from control to SuHx, with male masses higher than female. Data shown as mean ± SE. * $p < 0.05$ comparison between control and SuHx, # $p < 0.05$ comparison between sexes.

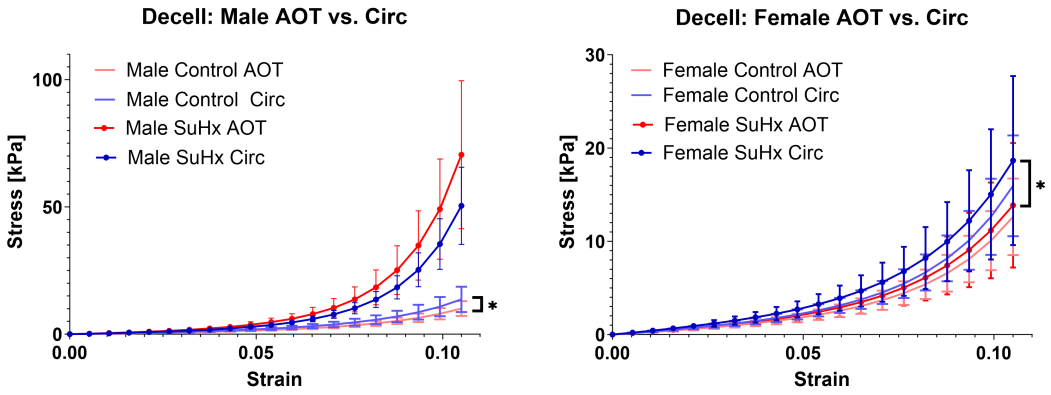

(a) (b)

Figure 8.15. Comparison of stiffness in the two axes: apex-outflow (AOT, red) and circumferential (Circ, blue) for decellularized tissues. Comparison is shown for Control (light) and SuHx Week 8 (dark) in (a) male and (b) female animals. Note the differences in y-axis scale between the two sub-figures. Data shown as mean ± SE. Male control and female SuHx groups both have significant difference between axes (* $p < 0.05$).

($p = 0.0070$), where the circumferential axis is stiffer than apex-outflow. This implies that the Cir axis stiffens more in females, as it is not significantly different from AOT in control, but is significantly stiffer in SuHx. Strain is a significant factor in all groups ($p < 0.0001$). Once again

to simplify further results, we will focus on the AOT axis, but the difference between axes in male control and female SuHx animals should be noted.

8.3.2 Male ECM Stiffness Increases in PAH

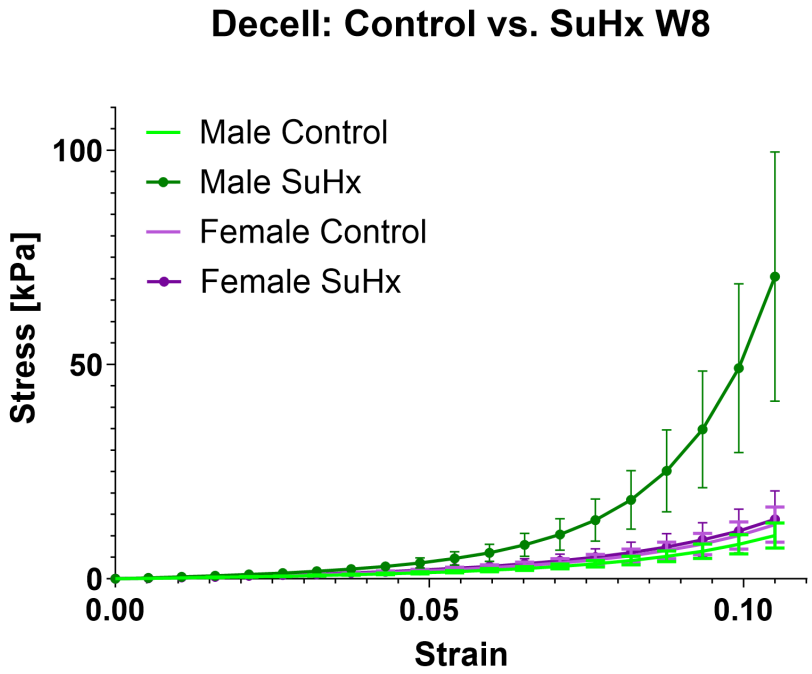

Figure 8.16. Average stress-strain curves for decellularized male (green) and female (purple) samples, control (light, solid) and SuHx Week 8 (dark, dotted). Male ECM is stiffer in SuHx than control; female retain low stresses. Data shown as mean $\pm$ SE.

Figure 8.16 shows averaged equibiaxial stress-strain curves for decellularized male and female tissues, both control and 8 weeks of SuHx. Males are seen to stiffen in PAH, with the SuHx group reaching higher stresses than the control group. Female SuHx and control curves are seen to reach similar stresses, with SuHx only marginally stiffer. Due to statistically significant interactions between sex, treatment, and strain in three-way ANCOVA, it was decided to run two-way ANCOVA for each sex separately, looking at effects of treatment and strain. With this comparison, the interaction between treatment and strain was significant for males ($p < 0.0001$), which is consistent with the observation that the Male SuHx curve is much steeper than the Male

Control curve. Females, however, do not have a significant interaction ($p = 0.2112$), and have significant differences due to both strain ($p < 0.0001$) and treatment ($p = 0.0305$).

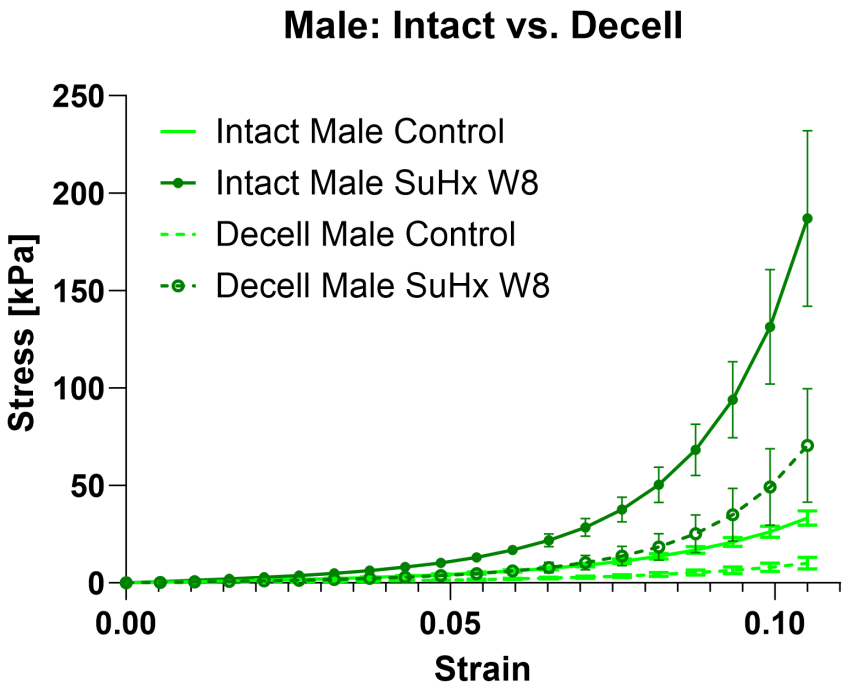

Figure 8.17. Average stress-strain curves for male rats, comparing intact (solid line) to decellularized (dashed line) samples for both control (light green) and SuHx (dark green, dotted). The intact myocardium is stiffer than the ECM for both control and SuHx animals. Data shown as mean $\pm$ SE. Due to significant interaction, no differences are statistically significant.

When comparing decellularized tissues to the intact myocardium from male rats, we see that the ECM is less stiff than the intact tissue for both control and SuHx groups (Figure 8.17). Figure 8.18 shows the same results in female rats, where both control and SuHx females have stiffer intact myocardium than decellularized ECM. Four-way ANCOVA found significant interactions between sex, treatment, tissue type (intact, decell), and strain, so the sex and treatment groups are analyzed individually do determine effect of decellularization. Separate two-way ANCOVAs testing tissue type and strain also found significant interactions ($p < 0.0001$) for all groups (Male Control, Male SuHx, Female Control, and Female SuHx).

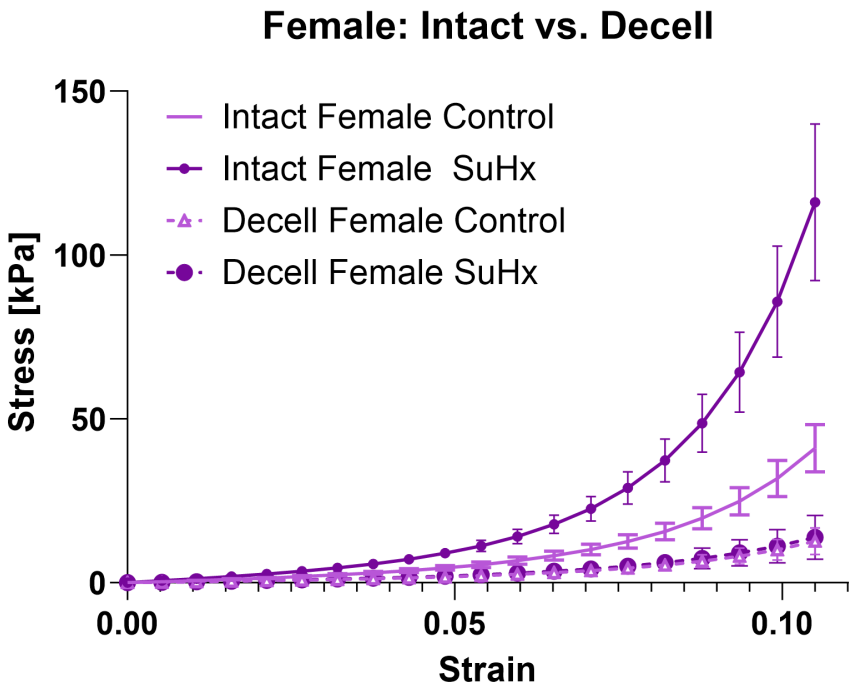

Figure 8.18. Average stress-strain curves for female rats, comparing intact (solid line) to decellularized (dashed line) samples for both control (light purple) and SuHx (dark purple, dotted). Myocardium from both control and SuHx females is stiffer than decellularized ECM. Data shown as mean $\pm$ SE. Due to significant interaction, no differences are statistically significant.

8.4 Collagen Content Increases in PAH

To further explore changes in the collagen ECM that occur in PAH, we quantified the amount of total collagen in tissue samples taken from distinct regions of the RV. These experiments were performed for male, intact female, and OVX female rats, both controls and at 8 weeks PAH development.

Figure 8.19 shows a heat map of collagen per tissue weight for the four regions of interest: top, left, bottom, and right (orientation defined in Section 3.4.1). Most regions are seen to increase from control to SuHx in all groups, an exception being the left region in OVX animals. Figure 8.20 shows that, when the four regions are viewed together for each group, male, intact female, and OVX female all increase from control to SuHx. Three-way ANOVA for group, treatment, and region found that group is significant ($p = 0.0038$), and there is significant

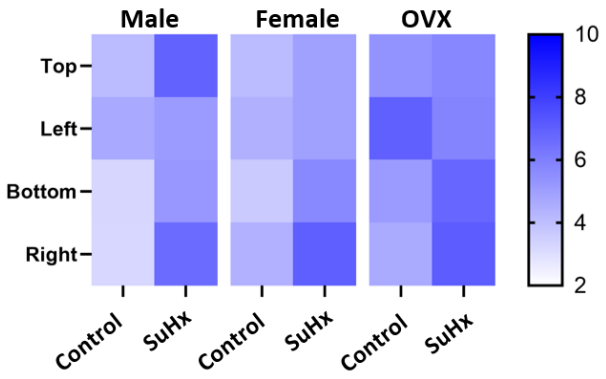

Figure 8.19. Heat map of regional total collagen content in Male, Female, and OVX control and SuHx rats. Rows represent RV region (top, left, bottom, or right), and columns represent animal categories (group and treatment). Color scale represents total collagen per tissue weight [ug/mg], where white/light to blue/dark denotes increase in mean collagen for group/region.

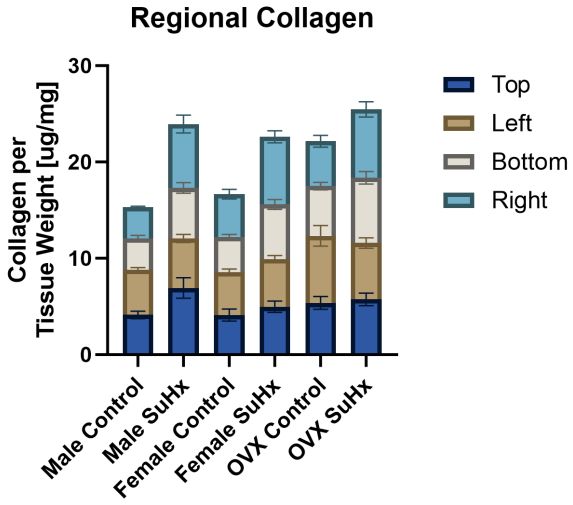

Figure 8.20. Bar graph showing total collagen per tissue weight in regions (top - dark blue, left - dark brown, bottom - light brown, and right - light blue) of the RV. Each column represents an animal category (group and treatment). Data shown as mean ± SE.

interaction between treatment and region ($p = 0.0032$). Tukey post-hoc test found significant differences when comparing OVX to female ($p = 0.0078$) and male ($p = 0.0162$), but male and female were not significantly different ($p = 0.9677$). When each region is analyzed separately with two-way ANOVA for group and treatment, the difference between SuHx and control is significant in the top ($p = 0.0470$), bottom ($p < 0.0001$), and right ($p < 0.0001$) regions.

Chapter 9

Discussion

SuHx induction and the subsequent development of PAH results in increased pulmonary arterial pressures and remodeling of the RV that affects both the morphology and passive mechanical properties of the myocardium. In this section, we discuss these changes as they occur over the progression of the disease and between sexes, both in the intact RV myocardium and in its decellularized collagen ECM.

9.1 RV Passive Stiffness in PAH Progression

We employed the well-established SuHx rat model of PAH to investigate the passive mechanical properties of the RV myocardium at three stages of disease development: Early (weeks 3, 4, and 6 post-SuHx induction), Mid (8 weeks post-induction), and Late (10, 12, and 15 weeks post-induction). This division of stages was determined based on previous research which used hemodynamic and morphological measurements to create a computational model of organ-level mechanics in the RV. The model from Kwan *et al.* computed material parameters for at end of diastole and systole from pressure-volume relations, which predicted mean passive stress-length relations for the sarcomere fibers and found the largest increase in stiffness from control to occur at 8 weeks of SuHx [14]. Our results confirm these findings in male rats, which we found to have the stiffest equibiaxial stress-strain relation in Mid-stage (week 8) PAH (Figure 8.6). Kwan *et al.* did not use female rats in the aforementioned study, but we found these same

results to occur for intact female rats (Figure 8.7). However, OVX female rats did not exhibit the same longitudinal stiffening pattern as is seen in males and intact females, instead peaking (only slightly) in the Late stage of PAH progression, with week 8 stiffening closely resembling Early-stage stiffening (Figure 8.8). This suggests a difference in the way SuHx-PAH progresses between surgically altered animals (OVX females) and intact animals (both males and females).

Despite SuHx Week 8 animals presenting with the highest mPAP for all sex groups, increases in RV thickness and mass that occur in hypertension do not share the same progression pattern over time. Figure 8.2 shows that, while intact female thickness peaks at 8 weeks of PAH, male thickness continues to increase through the Late stage, and OVX female thickness actually peaks in the Early stage. RV mass measurements (Figure 8.3) show the reverse trend in OVX females, where mass increases through the Late stage, whereas both male and intact female masses peak at week 8, similar to mPAP and stiffness. These comparisons suggest that changes in mass may be more indicative of changes in stiffness that occur over disease progression than changes in thickness or mPAP for OVX rats.

The decrease in average mPAP, mass, and stiffness that occurs after Week 8 in male and intact female SuHx rats is interesting, and the fact that OVX females see this shift from increasing to decreasing stiffness earlier in disease progression may suggest mechanisms of this change. We know that RV hypertrophy in PAH is at first adaptive and maintains cardiac output, then transitions to maladaptive with right heart failure, a process that is functionally characterized by decreased cardiac output with increased RV dilation and wall stress [9]. More increased stiffness and thickness in OVX females with Early-stage PAH compared to males and intact females indicates a more rapid and pronounced hypertrophic response to SuHx induction that is maintained throughout the disease progression, which may be related to the absence of ovarian hormones in female sex. Sex differences will be discussed in more detail in the following section.

The above discussion is based on findings from the apex-outflow axis of the RV free wall. We chose to focus on this direction following the finding that the tissue behavior is not anisotropic

in SuHx-PAH (Figure 8.5). However, it should be noted that there was a small (not statistically significant) difference in the two axes: apex-outflow direction is observed as slightly stiffer than circumferential for all sex groups during the disease. The only significant difference in axis stiffness occurred in male control rats, where again apex-outflow is stiffer than circumferential, and here the difference is still small. Similar studies have found that, contrary to our results, the RV free wall is anisotropic, though the direction and magnitude of this behavior varies between studies. Witzenburg *et al.* found that RV myocardium from normal (control) rats was roughly five times stiffer in the circumferential direction [35]. These results were reinforced by similar findings from Velez-Rendon *et al.*, who also found circumferential to be the stiffer of the two axes, though to a lesser extent [15]. Hill *et al.* and Valdez-Jasso *et al.* both found circumferential to be the less stiff axis [36] [37]. It is likely that the direction of stiffness is highly dependent on the precise orientation in which the RV free wall is tested, which is perhaps not consistent between the aforementioned studies. To attempt to explain this, we tested a tissue sample that was cut from the RV free wall at a roughly 45°angle from the usual orientation, and found that the tissue exhibited anisotropic behavior, with the adjusted-circumferential axis the stiffer (Figure 10.3). This reinforces the importance of precision and consistency in the preparation of tissue samples for mechanical testing, and highlights a need for thorough documentation in order to accurately compare studies.

9.2 Sex Differences in RV Passive Stiffness

PAH is a sexually dimorphic disease that is more common in women, but in which pre-menopausal women have better survival outcomes than men and post-menopausal women [16]-[20]. To incorporate differences due to sex in our study, we used both male and female rats, where females were studied both with and without ovaries (intact and OVX). We found that the increase in passive stiffness that occurs during RV remodeling in PAH is dependent on sex and ovaries, and that this dependence varies over the course of PAH progression.

Differences in stiffness between control animals from the three sex groups were not determined statistically significant, but we see that in health male RVs are the most compliant, and OVX female RVs are the least compliant, with the compliance of intact female RVs falling somewhere in the middle. In Early-stage PAH, we observed that males stiffen more than intact females, but that OVX females remain the stiffest (Figure 8.9). Then in week 8 of PAH, male stiffness exceeds that of OVX female, with intact female tissues still the most compliant (Figure 8.10). Finally, as the disease progresses to Late-stage, OVX females are once again the stiffest, with males still stiffer than intact females, which are again the most compliant (Figure 8.11).

If we remove OVX females from this analysis and look only at the influence of sex between our two unaltered groups, it is clear that males exhibit more pronounced stiffening than females at all stages of SuHx progression; females are stiffer in health but more compliant in disease than males at all time points. This aligns with clinical data which shows better disease outcomes for pre-menopausal female patients with PAH. It also aligns with the previous animal study from Lahm *et al.*, where the authors found that RV compliance decreases in SuHx, but females had more preserved compliance than males [22]. However, compliance in this study was determined from echocardiography and hemodynamic data, and *ex vivo* mechanical properties have not been previously published for female rats with SuHx PAH.

The differences in PAH between males and females appear to diminish between the ages of 45 and 65, suggesting that menopause may be a factor in female responses to the disease [18] [19]. OVX females were used in this study as a pseudo model of menopause, where compared to intact females they have reduced presence of ovarian hormones. Estrogen, specifically E2, has been implicated as an important modulator of the disease in previous animal studies; it has protective effects on RV function and attenuates some maladaptive processes seen in PAH [38] [22] [7] [8]. However, we do not test the biochemistry of estrogen, or link estrogen specifically to the mechanical properties measured in our study. OVX female rats are not completely void of estrogen, and estrogen levels vary across the stages of the estrous cycle in intact females [39]. That being said, OVX animals are still a valuable way to examine the RV adaptations

experienced by females with different ovarian statuses. As mentioned above, OVX females had stiffer stress-strain relations than females, both in health and in all stages of PAH. This is again in agreement with previous results from Lahm *et al.*, where the compliance in OVX females was seen to decrease to similar levels seen in males [22]. The mechanisms of this difference are unclear, but most likely do relate to estrogen, and further highlight a need for additional research towards solving the sex paradox.

9.3 ECM Contributions to RV Passive Stiffness

The RV free wall myocardium has two main components: myofibers and the ECM, which consists largely of collagen. To distinguish contributions to stiffening from the myofibers from those from the ECM, we decellularized samples of RV free wall that had been previously subjected to planar biaxial testing, and retested the resulting ECM.

An early observation from decellularized tissue stress-strain curves is that they exhibit more pronounced in-group variation than do the intact myocardium tissues, as can be seen by the outliers in Figure 8.12. No quantitative tests are done to the decellularized samples to confirm complete removal of non-ECM constituents, and this process is performed over a variable length of time that is subjective to visual observation from the researcher. Figure 3.3 shows a representative sample of RV undergoing decellularization, but not all samples become as completely transparent, perhaps due to insufficient time in SDS, or differences in the tissue itself. Additionally, some decellularized tissues are stored in refrigerated PBS for months before undergoing planar biaxial testing, and it is possible that these undergo changes during this storage period which alter the mechanical characteristics. Further analysis could be done to account for time in SDS and storage, but these factors were not considered in the current study.

Similar to the intact tissues, RV ECM was found to have significant anisotropic behavior in male control rats (Figure 8.15). While the difference in axes is again not significant in male SuHx, this difference was found to be significant in female SuHx ECM, where the circumferential

axis is stiffer than apex-outflow. The circumferential axis was observed as slightly less-stiff in intact SuHx tissues, so these results show the preferred axis switching between intact and decellularized samples. Once again, due to contradictory results in previous literature, it is hard to conclude whether anisotropic changes are due to fiber reorientation in SuHx, or due to differences in tissue orientation. Future imaging experiments could help elucidate the nature of these changes.

Figure 8.16 shows large increases in stiffness occurring in male, but not female, RV ECM. The lack of ECM stiffening in females is a surprising result, given both previous results on male ECM mechanics and the myocardial stiffening seen in the intact tissues from females. Female intact myocardium did not stiffen as much as male, but it did stiffen to a greater extent than its decellularized group shows. This suggests a possible explanation for the differential stiffening seen between male and female myocardium in PAH: the stiffening seen in females is entirely due to stiffening of the myofibers, whereas males have stiffness contributions from both the myofibers and the ECM. It is worth noting, however, that only 4 animals are included in the decellularized female SuHx group, so further experiments are needed to confirm these findings. We also did not include any data from decellularized OVX female samples, which may help better understand the role of the ECM in RV passive mechanics.

Since the ECM consists mainly of collagen, we decided to run additional experiments to quantify the total collagen content in pieces of RV myocardium. PAH has been shown to include increased collagen and RV fibrosis [12]. We found this to be the case in three out of four regions of the RV that were tested – collagen per tissue weight increased significantly in SuHx in all regions but the left (Figure 8.19). Interestingly, it has been observed during tissue preparation that the left side of the tissue is noticeable thicker than the right side. This suggests that regional thickness increase is likely due to greater myocyte hypertrophy, rather than increased collagen accumulation. Contrary to our findings, Kwan *et al.* previously found no significant change in RV free wall collagen content from control to SuHx [14]. Since we did see some regional differences in collagen content, it is possible that the tissue samples used in the Kwan *et al.* study

are not representative of regions in which collagen increases in PAH. It is also interesting to note the sex differences in collagen content. OVX females were significantly different than both males and intact females, having more collagen than both. However, males and females did not differ significantly, which complicates our previous observation that the female ECM does not stiffen in PAH. Since total collagen content is not significantly different between males and females, other factors such as organization and tortuosity may be responsible for the change in male ECM stiffness. Further studies may aim to characterize these differences and their relation to RV stiffening in PAH.

9.4 Limitations and Future Directions

The current study does not include data for mechanical properties of ECM from OVX female animals, so no conclusions can be made about the effect of ovarian hormones in ECM stiffening. Given the surprising results in female ECM, as well as the differences in collagen content in OVX animals compared to males and intact females, this would be an interesting group to study in future experiments. The current study also has limited sample sizes at some weeks of the disease, specifically in female ECM where only 4 animals were included. Improving these numbers would allow for higher confidence in the results observed, as well as open the possibility for separating the weeks from each disease stage. Since OVX female RVs have peak stiffness in the Late stage, we are unable to determine whether this happens at week 10, 12, or 15. The small sample sizes are in part due to large variation in stress-strain curves, which requires exclusion of some data that gives rise to a binomial distribution, as shown in Figure 8.12. When included, these outliers result in a group average that is not representative of any of the individual data. Part of the large in-group variation may come from the fact that not all tissues reach 10% strain in mechanical testing, so the model must extrapolate in order to generate stresses at higher strain values. Comparing at lower strains may be an alternative for future studies to investigate, but would lose some of the exponential behavior observed at higher strains.

A theoretical limitation of this study is that it uses the thin wall assumption, and this may not hold valid in some hypertensive RVs where the thickness becomes fairly large. Thickness is also assumed to be homogeneous across the RV wall, which is certainly not the case in some samples. Additionally, the current framework is unable to determine the contributions of the ECM to the overall myocardium, which would require a mixture model that accounts for changes in both the cell and matrix compartments of the tissue.

Future studies might aim to identify the underlying mechanisms of RV stiffening. We showed here that the RV myocardium and ECM stiffen in PAH, but that this stiffening differs between sexes, and within the female sex differs based on the presence of ovarian hormones. There may be collagen production pathways involved in PAH RV remodeling, and ovarian hormones may be involved in these pathways, or other pathways that regulate myocyte passive stiffening.

Chapter 10

Experimental Alternative Methods, and Other Applications

10.1 Alterations to the Planar Biaxial Testing Protocol

This chapter discusses the effect of modifying some of the protocols used in mechanical testing of the right ventricle, such as changes in chemical composition of the solution in which the tissue is submerged during testing. In addition, we discuss how these methods were adapted and used to study skeletal muscle of mice, and the main pulmonary artery of rats. Finally, a section will cover collagen quantification in the rat septal wall and uterus.

10.1.1 2D Isoparametric Triangular Linear Element Mapping

In order to evaluate the effects of analyzing strain computed from three markers rather than four, a new method for isoparametric mapping was implemented. Displacement vectors and the deformation gradient are computed as in Section 7.2.1, followed by mapping *via* a new, three-node set of shape functions:

$$N_1(s,r) = s$$

$$N_2(s,r) = r$$

$$N_3(s,r) = 1 - s - r$$

So that now the position vectors x and y can be described by:

$$x = \Sigma_{i=1}^{3} N_i(s,r)x_i$$

$$y = \Sigma_{i=1}^{3} N_i(s,r)y_i$$

This analysis method was applied to a selection of tissues that were previously analyzed using the four-marker mapping, and differences in the results were observed visually (Figure 10.1). It was determined that this method did not improve results and the triangle data was not used in any further analysis, but code can be found for any potential future use in the lab drive.

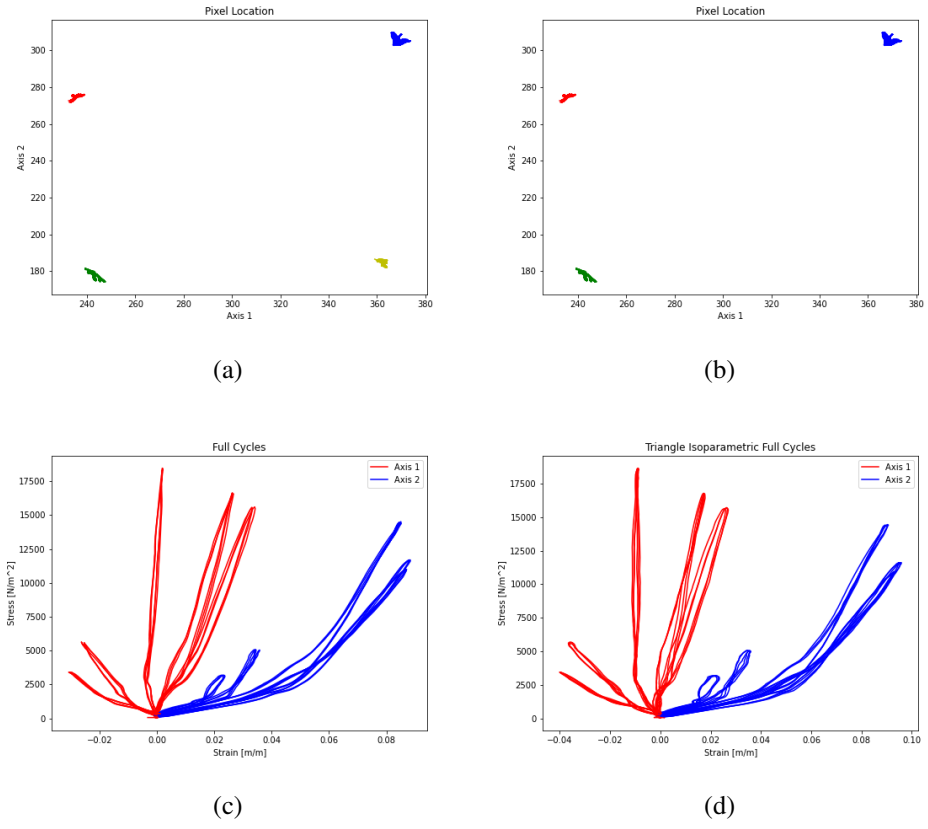

Figure 10.1. Example of results from triangle isoparametric mapping. Pixel positions with all four markers (a) and with the yellow marker excluded (b), and the corresponding stress-strain curves from these analyses (c) and (d). Data is from Female SuHx Rat 143, Trial 2.

10.1.2 The Effects of Rotating Tissue Sample

To explore an alternative orientation of anisotropy in the tissue sample we investigated the effect of rotated axes on the mechanical properties of the tissue. A male control rat was used for this experiment, and underwent the same invasive hemodynamic measurements detailed in Section 3.2 before excision of the RV free wall. Following excision, the tissue was aligned according to a rotated orientation, where the apex-outflow tract was identified as it usually is, then the tissue was rotated approximately 45°clockwise and cut into a square (Figure 10.2). The same biaxial testing protocol described in Section 5.2 was employed, with Axis 1 now representing a semi-longitudinal apex-inflow tract, and Axis 2 representing a semi-circumferential tract. Data from this test was processed and analyzed the same as other tissues. Figure 10.3 shows that Axis 2 (semi-circumferential) is stiffer than Axis 1. This test was only performed on one animal, but initial results indicate that the tissue behaves anisotropically in this orientation.

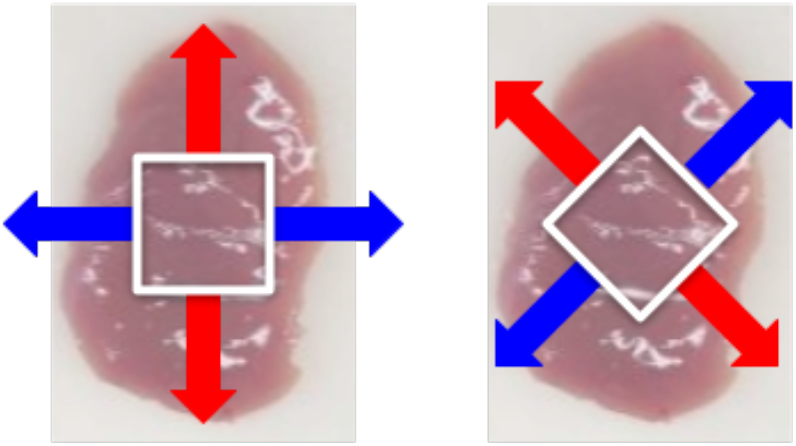

Figure 10.2. Schematic of original and rotated axes on the excised RV free wall. Original axes (left) are apex-outflow (red) and circumferential (blue). These were rotated approximately 45°in this experiment, resulting in a semi-longitudinal (red) and semi-circumferential (blue) axes.

10.1.3 Modification of Solution Composition During Mechanical Testing

To explore possible contractile effects in the tissue sample, a combination of Kreb's solution and 2,3-Butanedione monoxime (BDM) was used in the tissue preparation and/or biaxial

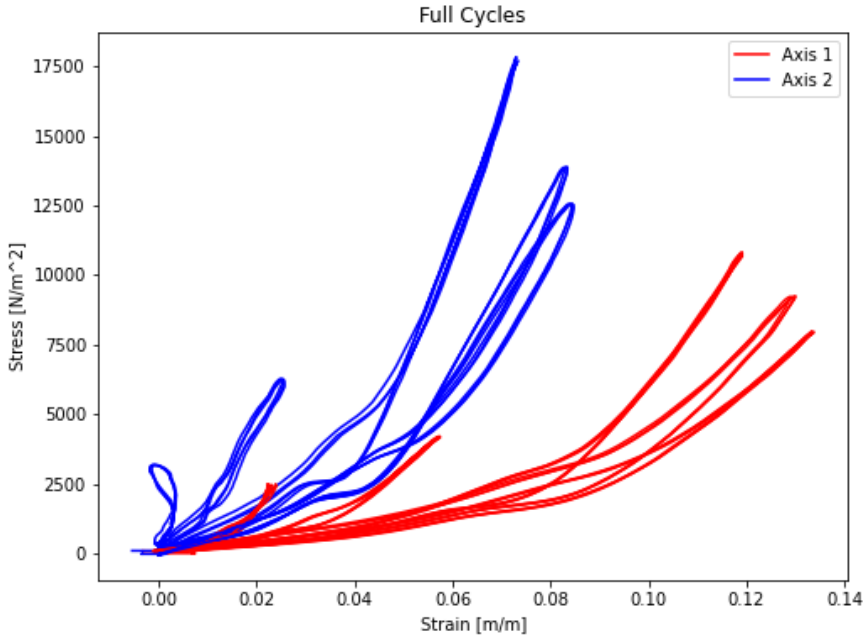

Figure 10.3. Stress-strain curves for a male control RV with a rotated orientation relative to other tissue squares used in this project. Axis 1 (blue) denotes a semi-longitudinal apex-inflow tract, and Axis 2 (red) represents a semi-circumferential tract. The tissue behavior is anisotropic, with Axis 2 stiffer than Axis 1.

testing portions of additional experiments performed on male control RVs. Kreb's solution is a balanced salt solution that provides cells with the moisture and salts needed for metabolism. BDM is a myosin inhibitor that prevents skeletal and cardiac muscle contractions. Two tissues were submerged in modified Kreb's solution with BDM and rocked for approximately 30 minutes at 4°C, before being mechanically tested while submerged in the normal 1x PBS solution at 36.5°C. The mechanical testing protocol was the same as detailed in Section 5.

An additional three tissues were mechanically tested with the bath filled with Kreb's solution, again following the usual protocol. One of these three tissues was soaked in BDM as described above prior to testing. An interesting note on experimental procedure for these tests: the bath became polluted with crystallized dextrose particles which floated on the surface of the solution and obscured the camera's tracking of the markers. A solution was improvised in which

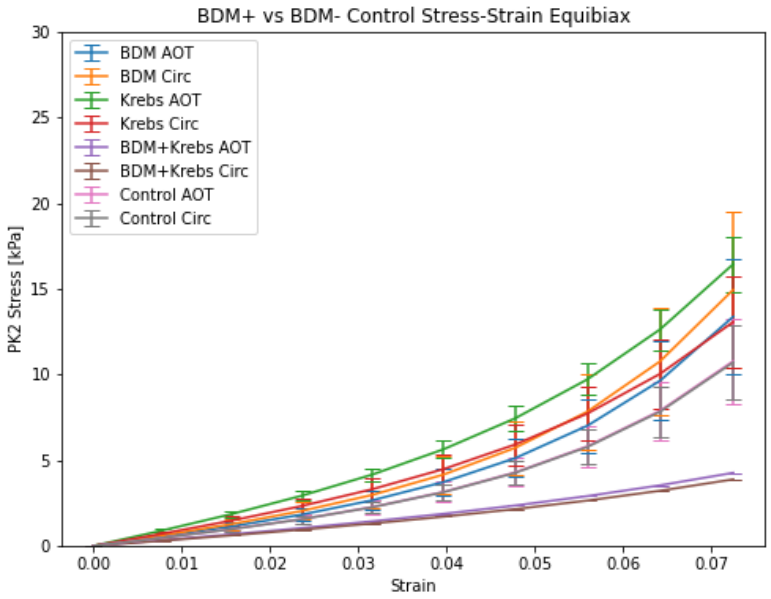

Figure 10.4. Equibiaxial stress-strain curves from the BDM/Kreb's solution experiments, compared to the average male control. Data is shown for both apex-outflow (AOT) and circumferential (Circ) axes, ± SE. BDM+Krebs tissues are slightly less stiff than control, and other modified tissues are slightly more stiff.

a petri dish, stabilized by beakers of tap water, was set on the surface of the solution below the camera, acting as a floating window to see into the solution. This allowed for successful marker tracking, and had no evident effects on the mechanical testing.

Data recorded from the five tissues mentioned above was analyzed using the regular code, and the resulting equibiaxial stress-strain curves were compared to the average from the male control group. We can see in Figure 10.4 that tissues treated with both BDM and Kreb's are slightly less stiff than control, and other modified tissues are slightly more stiff.

10.2 Other Applications

10.2.1 Planar Biaxial Testing of Mouse Skeletal Muscle

As part of the Wu Tsai Human Performance Alliance, I assisted Katie Knaus in performing planar biaxial mechanical testing of mouse skeletal muscle. Mouse biceps femoris was

excised, and the side lengths and thickness of the muscle was measured by digital caliper. Five markers were glued to the surface of the tissue, and 12 custom-made hooks were inserted through the edges (four on each long edge, two on each short edge). The muscle was then subjected to planar biaxial mechanical testing in the along-fiber and cross-fiber directions, using a unique testing protocol created by Katie Knaus. Subsequent analysis was performed using a script adjusted from the normal code.

10.2.2 Planar Biaxial Testing of the Main Pulmonary Artery

To supplement mechanical characterization of the pulmonary artery done via tubular biaxial testing by Vaishali Harimani, I performed planar biaxial testing of a main pulmonary artery. Two right pulmonary artery samples were tested by first opening and measuring the artery, then applying markers and mechanically stretching with the same protocol used for intact myocardium. Preliminary results were analyzed by Vaishali Harimani using a modified version of the normal analysis code.

10.2.3 Collagen Quantification in Septum and Uterus

As part of our investigation of the collagen content in various sections of the RV, we ran a small set of similar tests on samples of rat septum and uterus. This was a proof-of-concept test to determine whether useful information could be gained from running the same experimental protocol on these tissue types. The collagen assay procedure was identical to that detailed in Section 3.4.2, with slight differences in the preceding tissue preparation steps that were necessary due to inherent differences in the tissue sources. Briefly, septum pieces were isolated from previously-frozen samples by first removing the left ventricle (in cases where it was not previously removed) and then slicing a small piece of tissue from near the center of the septum wall. Similarly, uterus samples that had been previously frozen were thawed, and a small piece was cut from the uterine horn, near the cervix (Figure 10.5). We were unable to distinguish from which horn (left versus right) the sample was cut due to lack of identifiable orientation.

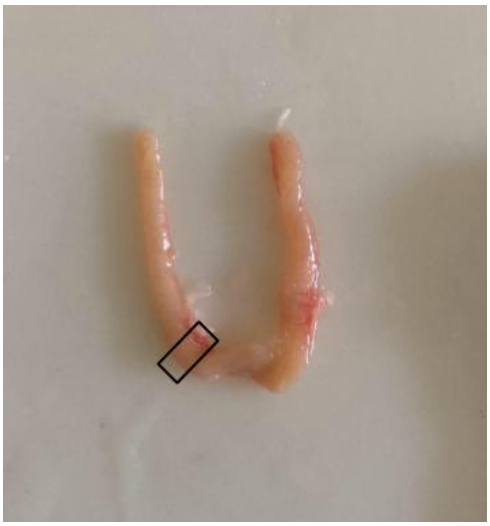

Figure 10.5. Excised rat uterus, with black box marking the approximate region of the uterine horn from which tissue sample was taken for collagen assay.

Data collected from this experiment was analyzed the same as previously described in Section 3.4.3. Results revealed that both the septum and uterus have higher collagen content than does the RV, and an altered test protocol (where either diluted samples or a higher collagen standard is used) is necessary to make valid conclusions about collagen content in these tissues. However, this was an interesting experiment that provided some preliminary data and proof-of-concept for further investigation.

Bibliography

[1] G. Simonneau, D. Montani, D. S. Celermajer, C. P. Denton, M. A. Gatzoulis, M. Krowka, P. G. Williams, and R. Souza, "Haemodynamic definitions and updated clinical classification of pulmonary hypertension," *European Respiratory Journal*, vol. 53, no. 1, 2019. [Online]. Available: https://erj.ersjournals.com/content/53/1/1801913

[2] Y.-C. Lai, K. C. Potoka, H. C. Champion, A. L. Mora, and M. T. Gladwin, "Pulmonary arterial hypertension: the clinical syndrome," *Circulation Research*, vol. 115, no. 1, pp. 115–130, Jun. 2014. [Online]. Available: https://www.ncbi.nlm.nih.gov/pmc/articles/PMC4096686/

[3] G. M. O'Leary, "Pulmonary arterial hypertension: An overview," *Nursing*, vol. 51, no. 11, pp. 37–43, Nov. 2021. [Online]. Available: https://pubmed.ncbi.nlm.nih.gov/34678820/

[4] L. Leber, A. Beaudet, and A. Muller, "Epidemiology of pulmonary arterial hypertension and chronic thromboembolic pulmonary hypertension: identification of the most accurate estimates from a systematic literature review," *Pulmonary Circulation*, vol. 11, no. 1, p. 2045894020977300, Jan. 2021. [Online]. Available: https://www.ncbi.nlm.nih.gov/pmc/articles/PMC7797595/

[5] M. Y. Farhat, M. F. Chen, T. Bhatti, A. Iqbal, S. Cathapermal, and P. W. Ramwell, "Protection by oestradiol against the development of cardiovascular changes associated with monocrotaline pulmonary hypertension in rats." *British Journal of Pharmacology*, vol. 110, no. 2, pp. 719–723, Oct. 1993. [Online]. Available: https://www.ncbi.nlm.nih.gov/pmc/articles/PMC2175952/

[6] S. Umar, A. Iorga, H. Matori, R. D. Nadadur, J. Li, F. Maltese, A. van der Laarse, and M. Eghbali, "Estrogen Rescues Preexisting Severe Pulmonary Hypertension in Rats," *American Journal of Respiratory and Critical Care Medicine*, vol. 184, no. 6, pp. 715–723, Sep. 2011. [Online]. Available: https://www.ncbi.nlm.nih.gov/pmc/articles/PMC3208600/

[7] A. L. Frump, K. N. Goss, A. Vayl, M. Albrecht, A. Fisher, R. Tursunova, J. Fierst, J. Whitson, A. R. Cucci, M. B. Brown, and T. Lahm, "Estradiol improves right ventricular function in rats with severe angioproliferative pulmonary hypertension: effects of endogenous and exogenous sex hormones," *American Journal of Physiology. Lung Cellular and Molecular Physiology*, vol. 308, no. 9, pp. L873–890, May 2015.

[8] A. L. Frump, M. Albrecht, B. Yakubov, S. Breuils-Bonnet, V. Nadeau, E. Tremblay, F. Potus, J. Omura, T. Cook, A. Fisher, B. Rodriguez, R. D. Brown, K. R. Stenmark, C. D. Rubinstein, K. Krentz, D. M. Tabima, R. Li, X. Sun, N. C. Chesler, S. Provencher, S. Bonnet, and T. Lahm, "17-Estradiol and estrogen receptor protect right ventricular function in pulmonary hypertension via BMPR2 and apelin," *The Journal of Clinical Investigation*, vol. 131, no. 6, p. e129433, 2021. [Online]. Available: https://www.ncbi.nlm.nih.gov/pmc/articles/PMC7968046/

[9] A. L. Frump, S. Bonnet, V. A. de Jesus Perez, and T. Lahm, "Emerging role of angiogenesis in adaptive and maladaptive right ventricular remodeling in pulmonary hypertension," *American Journal of Physiology - Lung Cellular and Molecular Physiology*, vol. 314, no. 3, pp. L443–L460, Mar. 2018. [Online]. Available: https://www.ncbi.nlm.nih.gov/pmc/articles/PMC5900357/

[10] D. Sharifi Kia, K. Kim, and M. A. Simon, "Current Understanding of the Right Ventricle Structure and Function in Pulmonary Arterial Hypertension," *Frontiers in Physiology*, vol. 12, p. 641310, May 2021. [Online]. Available: https://www.ncbi.nlm.nih.gov/pmc/articles/PMC8194310/

[11] P. Trip, S. Rain, M. L. Handoko, C. v. d. Bruggen, H. J. Bogaard, J. T. Marcus, A. Boonstra, N. Westerhof, A. Vonk-Noordegraaf, and F. S. d. Man, "Clinical relevance of right ventricular diastolic stiffness in pulmonary hypertension," *European Respiratory Journal*, vol. 45, no. 6, pp. 1603–1612, Jun. 2015. [Online]. Available: https://erj.ersjournals.com/content/45/6/1603

[12] S. Rain, M. L. Handoko, P. Trip, C. T.-J. Gan, N. Westerhof, G. J. Stienen, W. J. Paulus, C. A. Ottenheijm, J. T. Marcus, P. Dorfmüller, C. Guignabert, M. Humbert, P. MacDonald, C. dos Remedios, P. E. Postmus, C. Saripalli, C. G. Hidalgo, H. L. Granzier, A. Vonk-Noordegraaf, J. van der Velden, and F. S. de Man, "Right Ventricular Diastolic Impairment in Patients With Pulmonary Arterial Hypertension," *Circulation*, vol. 128, no. 18, pp. 2016–2025, Oct. 2013, publisher: American Heart Association. [Online]. Available: https://www.ahajournals.org/doi/10.1161/CIRCULATIONAHA.113.001873

[13] S. Rain, S. Andersen, A. Najafi, J. Gammelgaard Schultz, D. da Silva Gonçalves Bós, M. L. Handoko, H.-J. Bogaard, A. Vonk-Noordegraaf, A. Andersen, J. van der Velden, C. A. Ottenheijm, and F. S. de Man, "Right Ventricular Myocardial Stiffness in Experimental Pulmonary Arterial Hypertension," *Circulation. Heart Failure*, vol. 9, no. 7, p. e002636, Jul. 2016. [Online]. Available: https://www.ncbi.nlm.nih.gov/pmc/articles/PMC4956674/

[14] E. D. Kwan, D. Vélez-Rendón, X. Zhang, H. Mu, M. Patel, E. Pursell, J. Stowe, and D. Valdez-Jasso, "Distinct time courses and mechanics of right ventricular hypertrophy and diastolic stiffening in a male rat model of pulmonary arterial hypertension," *American Journal of Physiology. Heart and Circulatory Physiology*, vol. 321, no. 4, pp. H702–H715, Oct. 2021.

[15] D. Vélez-Rendón, E. R. Pursell, J. Shieh, and D. Valdez-Jasso, "Relative Contributions of Matrix and Myocytes to Biaxial Mechanics of the Right Ventricle in Pulmonary Arterial Hypertension," *Journal of Biomechanical Engineering*, vol. 141, no. 091011, Aug. 2019. [Online]. Available: https://doi.org/10.1115/1.4044225

[16] S. Rich, D. R. Dantzker, S. M. Ayres, E. H. Bergofsky, B. H. Brundage, K. M. Detre, A. P. Fishman, R. M. Goldring, B. M. Groves, and S. K. Koerner, "Primary pulmonary hypertension. A national prospective study," *Annals of Internal Medicine*, vol. 107, no. 2, pp. 216–223, Aug. 1987.

[17] D. B. Badesch, G. E. Raskob, C. G. Elliott, A. M. Krichman, H. W. Farber, A. E. Frost, R. J. Barst, R. L. Benza, T. G. Liou, M. Turner, S. Giles, K. Feldkircher, D. P. Miller, and M. D. McGoon, "Pulmonary Arterial Hypertension: Baseline Characteristics From the REVEAL Registry," *Chest*, vol. 137, no. 2, pp. 376–387, Feb. 2010. [Online]. Available: https://www.sciencedirect.com/science/article/pii/S0012369210600827

[18] A. Foderaro and C. E. Ventetuolo, "Pulmonary Arterial Hypertension and the Sex Hormone Paradox," *Current Hypertension Reports*, vol. 18, no. 11, p. 84, Nov. 2016. [Online]. Available: https://doi.org/10.1007/s11906-016-0689-7

[19] J. Hester, C. Ventetuolo, and T. Lahm, "Sex, Gender, and Sex Hormones in Pulmonary Hypertension and Right Ventricular Failure," *Comprehensive Physiology*, vol. 10, no. 1, pp. 125–170, Dec. 2019. [Online]. Available: https://www.ncbi.nlm.nih.gov/pmc/articles/PMC7338988/

[20] T. Lahm, R. M. Tuder, and I. Petrache, "Progress in solving the sex hormone paradox in pulmonary hypertension," *American Journal of Physiology-Lung Cellular and Molecular Physiology*, vol. 307, no. 1, pp. L7–L26, Jul. 2014, publisher: American Physiological Society. [Online]. Available: https://journals.physiology.org/doi/full/10.1152/ajplung.00337.2013

[21] C. E. Ventetuolo, P. Ouyang, D. A. Bluemke, H. Tandri, R. G. Barr, E. Bagiella, A. R. Cappola, M. R. Bristow, C. Johnson, R. A. Kronmal, J. R. Kizer, J. A. C. Lima, and S. M. Kawut, "Sex Hormones Are Associated with Right Ventricular Structure and Function," *American Journal of Respiratory and Critical Care Medicine*, vol. 183, no. 5, pp. 659–667, Mar. 2011. [Online]. Available: https://www.ncbi.nlm.nih.gov/pmc/articles/PMC3081282/

[22] T. Lahm, A. L. Frump, M. E. Albrecht, A. J. Fisher, T. G. Cook, T. J. Jones, B. Yakubov, J. Whitson, R. K. Fuchs, A. Liu, N. C. Chesler, and M. B. Brown, "17-Estradiol mediates superior adaptation of right ventricular function to acute strenuous exercise in female rats with severe pulmonary hypertension," *American Journal of Physiology-Lung Cellular and Molecular Physiology*, vol. 311, no. 2, pp. L375–L388, Aug. 2016, publisher: American Physiological Society. [Online]. Available: https://journals.physiology.org/doi/full/10.1152/ajplung.00132.2016

[23] O. Boucherat, V. Agrawal, A. Lawrie, and S. Bonnet, "The Latest in Animal Models of Pulmonary Hypertension and Right Ventricular Failure," *Circulation Research*, vol.

130, no. 9, pp. 1466–1486, Apr. 2022, publisher: American Heart Association. [Online]. Available: https://www.ahajournals.org/doi/10.1161/CIRCRESAHA.121.319971

[24] A. Hautefort, P. Mendes-Ferreira, J. Sabourin, G. Manaud, T. Bertero, C. Rucker-Martin, M. Riou, R. Adão, B. Manoury, M. Lambert, A. Boet, F. Lecerf, V. Domergue, C. Brás-Silva, A. M. Gomez, D. Montani, B. Girerd, M. Humbert, F. Antigny, and F. Perros, "Bmpr2 Mutant Rats Develop Pulmonary and Cardiac Characteristics of Pulmonary Arterial Hypertension," *Circulation*, vol. 139, no. 7, pp. 932–948, Feb. 2019.

[25] N. S. Hill, M. N. Gillespie, and I. F. McMurtry, "Fifty Years of Monocrotaline-Induced Pulmonary Hypertension: What Has It Meant to the Field?" *CHEST*, vol. 152, no. 6, pp. 1106–1108, Dec. 2017, publisher: Elsevier. [Online]. Available: https://journal.chestnet.org/article/S0012-3692(17)32899-4/abstract

[26] Y. Kasahara, R. M. Tuder, L. Taraseviciene-Stewart, T. D. Le Cras, S. Abman, P. K. Hirth, J. Waltenberger, and N. F. Voelkel, "Inhibition of VEGF receptors causes lung cell apoptosis and emphysema," *The Journal of Clinical Investigation*, vol. 106, no. 11, pp. 1311–1319, Dec. 2000.

[27] L. Taraseviciene-Stewart, Y. Kasahara, L. Alger, P. Hirth, G. Mc Mahon, J. Waltenberger, N. F. Voelkel, and R. M. Tuder, "Inhibition of the VEGF receptor 2 combined with chronic hypoxia causes cell death-dependent pulmonary endothelial cell proliferation and severe pulmonary hypertension," *FASEB journal: official publication of the Federation of American Societies for Experimental Biology*, vol. 15, no. 2, pp. 427–438, Feb. 2001.

[28] K. Abe, M. Toba, A. Alzoubi, M. Ito, K. A. Fagan, C. D. Cool, N. F. Voelkel, I. F. McMurtry, and M. Oka, "Formation of plexiform lesions in experimental severe pulmonary arterial hypertension," *Circulation*, vol. 121, no. 25, pp. 2747–2754, Jun. 2010.

[29] M. Toba, A. Alzoubi, K. D. O'Neill, S. Gairhe, Y. Matsumoto, K. Oshima, K. Abe, M. Oka, and I. F. McMurtry, "Temporal hemodynamic and histological progression in Sugen5416/hypoxia/normoxia-exposed pulmonary arterial hypertensive rats," *American Journal of Physiology - Heart and Circulatory Physiology*, vol. 306, no. 2, pp. H243–H250, Jan. 2014. [Online]. Available: https://www.ncbi.nlm.nih.gov/pmc/articles/PMC3920132/

[30] M. S. Sacks, "Biaxial Mechanical Evaluation of Planar Biological Materials," *Journal of elasticity and the physical science of solids*, vol. 61, no. 1, pp. 199–246, Jul. 2000. [Online]. Available: https://doi.org/10.1023/A:1010917028671

[31] Y. Lanir and Y. C. Fung, "Two-dimensional mechanical properties of rabbit skin. I. Experimental system," *Journal of Biomechanics*, vol. 7, no. 1, pp. 29–34, Jan. 1974.

[32] ——, "Two-dimensional mechanical properties of rabbit skin—II. Experimental results," *Journal of Biomechanics*, vol. 7, no. 2, pp. 171–182, Mar. 1974. [Online]. Available: https://www.sciencedirect.com/science/article/pii/002192907490058X

[33] P. Tong and Y. C. Fung, "The stress-strain relationship for the skin," *Journal of Biomechanics*, vol. 9, no. 10, pp. 649–657, 1976. [Online]. Available: https://pubmed.ncbi.nlm.nih.gov/965417/

[34] F. C. Yin, "Ventricular wall stress." *Circulation Research*, vol. 49, no. 4, Oct. 1981. [Online]. Available: https://www.ahajournals.org/doi/epdf/10.1161/01.RES.49.4.829

[35] C. Witzenburg, R. Raghupathy, S. M. Kren, D. A. Taylor, and V. H. Barocas, "Mechanical changes in the rat right ventricle with decellularization," *Journal of Biomechanics*, vol. 45, no. 5, pp. 842–849, Mar. 2012.

[36] M. R. Hill, M. A. Simon, D. Valdez-Jasso, W. Zhang, H. C. Champion, and M. S. Sacks, "Structural and Mechanical Adaptations of Right Ventricle Free Wall Myocardium to Pressure Overload," *Annals of Biomedical Engineering*, vol. 42, no. 12, pp. 2451–2465, Dec. 2014. [Online]. Available: https://doi.org/10.1007/s10439-014-1096-3

[37] D. Valdez-Jasso, M. A. Simon, H. C. Champion, and M. S. Sacks, "A murine experimental model for the mechanical behaviour of viable right-ventricular myocardium," *The Journal of Physiology*, vol. 590, no. Pt 18, pp. 4571–4584, Sep. 2012. [Online]. Available: https://www.ncbi.nlm.nih.gov/pmc/articles/PMC3477758/

[38] T. Lahm, M. Albrecht, A. J. Fisher, M. Selej, N. G. Patel, J. A. Brown, M. J. Justice, M. B. Brown, M. Van Demark, K. M. Trulock, D. Dieudonne, J. G. Reddy, R. G. Presson, and I. Petrache, "17-Estradiol Attenuates Hypoxic Pulmonary Hypertension via Estrogen Receptor–mediated Effects," *American Journal of Respiratory and Critical Care Medicine*, vol. 185, no. 9, pp. 965–980, May 2012. [Online]. Available: https://www.ncbi.nlm.nih.gov/pmc/articles/PMC3359941/

[39] A. A. Shaikh, "Estrone and Estradiol Levels in the Ovarian Venous Blood from Rats During the Estrous Cycle and Pregnancy*," *Biology of Reproduction*, vol. 5, no. 3, pp. 297–307, Dec. 1971. [Online]. Available: https://doi.org/10.1093/biolreprod/5.3.297